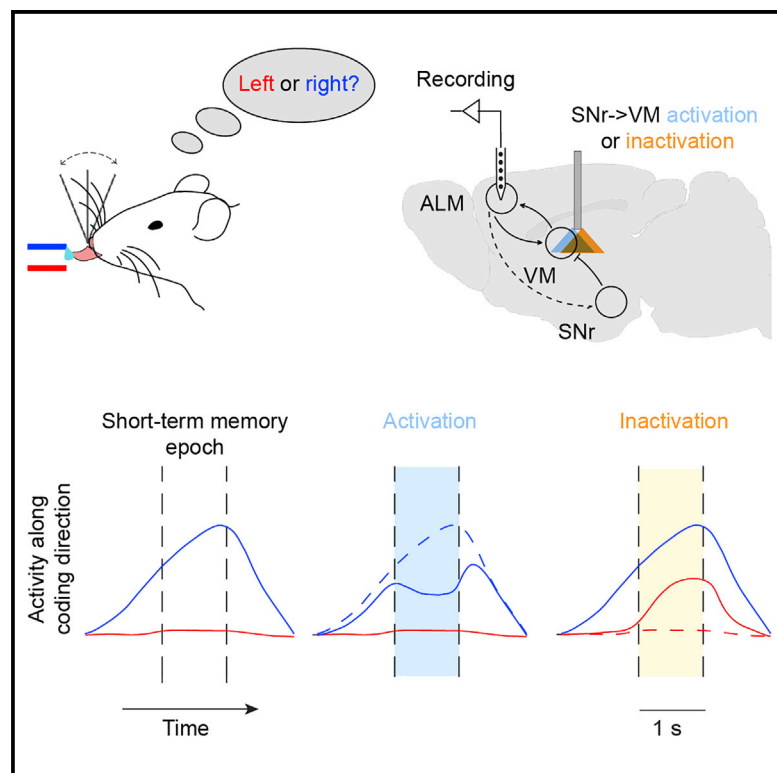


A cortico-basal ganglia-thalamo-cortical channel underlying short-term memory

Graphical abstract



Authors

Yu Wang, Xinxin Yin, Zhouzhou Zhang, Jiejue Li, Wenyu Zhao, Zengcai V. Guo

Correspondence

guozengcai@tsinghua.edu.cn

In brief

Short-term memory (STM)-related neural activity is distributed in multiple brain areas. How these brain areas interact to generate selective activity remains poorly understood. Wang et al. find that the cortico-basal ganglia-thalamo-cortical loop promotes selective activity underlying STM.

Highlights

- The SNr-to-thalamus pathway is causally involved in short-term memory
- Perturbation of the SNr-to-thalamus projection selectively modulates frontal activity
- Selectivity in the SNr is widely distributed but has a hotspot
- Perturbation of the frontal cortex selectively modulates SNr activity

Article

A cortico-basal ganglia-thalamo-cortical channel underlying short-term memory

Yu Wang,^{1,2,4} Xinxin Yin,^{1,2,4} Zhouzhou Zhang,^{1,3} Jiejue Li,^{1,2} Wenyu Zhao,^{1,2} and Zengcai V. Guo^{1,2,5,*}

¹IDG/McGovern Institute for Brain Research, School of Medicine, Tsinghua University, Beijing, China 100084

²Tsinghua-Peking Joint Center for Life Sciences, Beijing, China 100084

³School of Life Sciences, Tsinghua University, Beijing, China 100084

⁴These authors contributed equally

⁵Lead contact

*Correspondence: guozengcai@tsinghua.edu.cn

<https://doi.org/10.1016/j.neuron.2021.08.002>

SUMMARY

Persistent activity underlying short-term memory encodes sensory information or instructs specific future movement and, consequently, has a crucial role in cognition. Despite extensive study, how the same set of neurons respond differentially to form selective persistent activity remains unknown. Here, we report that the cortico-basal ganglia-thalamo-cortical (CBTC) circuit supports the formation of selective persistent activity in mice. Optogenetic activation or inactivation of the basal ganglia output nucleus substantia nigra pars reticulata (SNr)-to-thalamus pathway biased future licking choice, without affecting licking execution. This perturbation differentially affected persistent activity in the frontal cortex and selectively modulated neural trajectory that encodes one choice but not the other. Recording showed that SNr neurons had selective persistent activity distributed across SNr, but with a hotspot in the mediolateral region. Optogenetic inactivation of the frontal cortex also differentially affected persistent activity in the SNr. Together, these results reveal a CBTC channel functioning to produce selective persistent activity underlying short-term memory.

INTRODUCTION

Short-term memory (STM) is the ability of the brain to hold information internally in the absence of sustained sensory input and, thus, has a crucial role in working memory, decision making, motor planning, and action timing (Erlich et al., 2011; Fuster and Alexander, 1971; Gold and Shadlen, 2007; Guo et al., 2014b; Murakami et al., 2014; Tanji and Evarts, 1976). During STM, neurons show sustained elevated or suppressed firing, i.e., persistent activity (Funahashi et al., 1989; Fuster and Alexander, 1971; Romo et al., 1999; Tanji and Evarts, 1976). Neurophysiology from behaving animals and MRI studies from human subjects during the past half century have identified persistent activity distributed across various cortical and subcortical areas, including the prefrontal cortex, parietal cortex, premotor cortex, motor cortex, thalamus, basal ganglia, and cerebellum (Christophel et al., 2017; Curtis and Lee, 2010; Dotson et al., 2018; Erlich et al., 2011; Fuster and Alexander, 1971; Gao et al., 2018; Guo et al., 2017; Hikosaka and Wurtz, 1983; Liu et al., 2014; Pinto et al., 2019; Tanji and Evarts, 1976). Neurons in these areas show different levels of activation, i.e., selective persistent activity, which encodes behavioral variables related to sensory stimulus or motor planning (Dotson et al., 2018; Erlich et al., 2011; Funahashi et al., 1989; Gao et al., 2018; Guo

et al., 2014b, 2017; Hikosaka and Wurtz, 1983; Pinto et al., 2019; Romo et al., 1999; Tanji and Evarts, 1976). Persistent activity has the distributed nature involving a network of brain regions (Christophel et al., 2017; Svoboda and Li, 2018), but how multiple areas interact to promote selective persistent activity remains unknown.

The mouse anterior lateral motor cortex (ALM) has a causal role for STM in a tactile-based decision-making task (Guo et al., 2014b). A large fraction of ALM neurons exhibits persistent activity that predicts future licking directions (Guo et al., 2014b; Li et al., 2015). Thus, persistent activity underlying the STM represents prospective information about motor planning (Svoboda and Li, 2018). Persistent activity in the ALM depends on the reciprocal connections with the thalamus (including the ventral medial [VM] and parts of the ventral anterior-lateral [VAL] nuclei) (Guo et al., 2017). As the VM and the rostromedial portion of the VAL receive intense afferents from the substantia nigra pars reticulata (SNr) (Kuramoto et al., 2011; McElvain et al., 2021), we focus on the cortico-basal ganglia-thalamo-cortical (CBTC) circuit. The circuit has been implicated in action selection (Mink, 2003), timing of action initiation (Buhusi and Meck, 2005), and motor learning (Graybiel, 2008). Dysfunction of the circuit causes severe movement disorders, such as Parkinson and Huntington

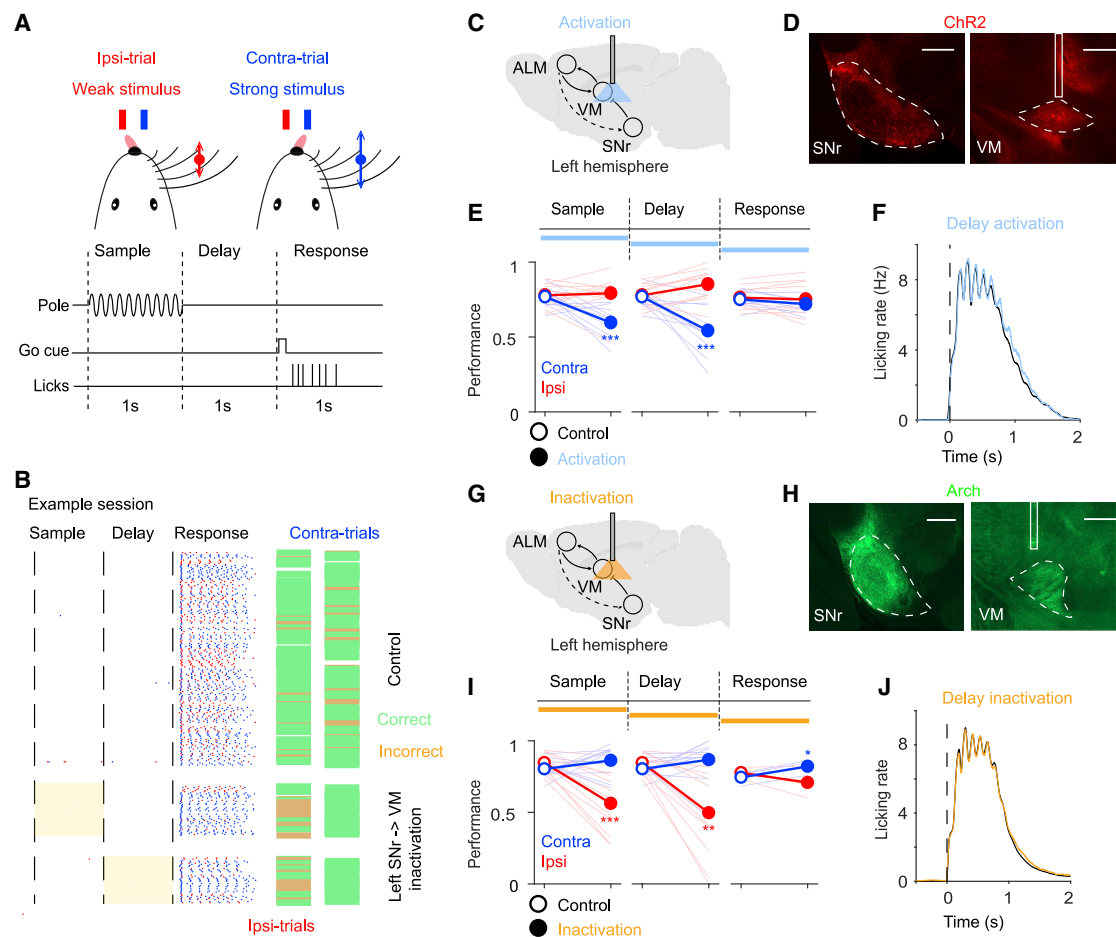


Figure 1. The SNr-to-thalamus pathway is critical for short-term memory

(A) Head-fixed mice report the stimulus strength by directional licking. Top: schematic of the task. Bottom: task structure. A pole vibrated with a large or small amplitude during the sample epoch. Mice responded with directional licking after a delay and an auditory go cue. Contra and ipsi denote the side relative to the optogenetically perturbed left hemisphere.

(B) Example behavioral session. Blue, contra-licks; red, ipsi-licks. Shading, inactivation of the SNr-to-thalamus projections. Right, trial outcome; green dash, correct; orange dash, incorrect.

(C) Schematic of the cortico-basal ganglia-thalamo-cortical pathway and optogenetic activation of SNr projections in the thalamus near the VM.

(D) Fluorescence image showing Cre-dependent ChR2 expression in SNr and axonal terminals in the VM. Solid white line, optical fiber location. Scale bar, 500 μ m. (E) Optogenetic activation of SNr-to-VM axons during the sample or delay epoch produces an ipsilateral bias ($n = 12$ mice). Each line represents a mouse (Method details). *** $p < 0.001$, t test.

(F) Licking rate during the response epoch after delay epoch activation. Black line, control.

(G) Schematic of optogenetic inactivation of SNr projections in the thalamus near the VM.

(H) Fluorescence image showing Cre-dependent Arch expression in the SNr and axonal terminals in the VM. Solid white line, optical fiber location. Scale bar, 500 μ m.

(I) Optogenetic inactivation of SNr-to-VM projections during the sample or delay epoch produces a contralateral bias ($n = 11$ mice). Each line represents a mouse (Method details). t test; *** $p < 0.001$, ** $p < 0.01$, * $p < 0.05$.

(J) Licking rate during the response epoch after the delay epoch inactivation. Black line, control.

See also Figure S1 and S2.

diseases (Graybiel, 2008; Kravitz et al., 2010; Mink, 2003), highlighting its role in motor functions. However, the role of the basal ganglia-thalamo-cortical pathway in cognitive functions remains elusive. Combining optogenetic perturbation, multichannel recording, and quantitative mouse behavior, we show that the CBTC circuit differentiates cortical neural trajectories underlying different STMs in different trial types, revealing its critical role in cognitive functions.

RESULTS

The basal ganglia-to-thalamus pathway is required for STM

Mice performed a tactile-based decision-making task with a STM component (Method details) (Figures 1A and 1B). In each trial, mice discriminated the strength of a vibrating stimulus with their whiskers during the sample epoch (lasting 1.0 s).

During the subsequent delay epoch (1.0 s, i.e., STM epoch), mice held the memory of the previous sensory experience and planned an upcoming directional licking. Following an auditory “go” cue, mice reported the stimulus strength with directional licking (left or right). Mice performed the task according to the stimuli strength (performance $77.8\% \pm 1.4\%$; lick-early before-go cue $7.6\% \pm 1.7\%$, and no-response rate $1.8\% \pm 0.7\%$; means \pm SEM; **Figures S1A–S1C**). The task is whisker dependent because trimming of the whiskers rendered the performance at chance level (**Figure S1D**). During the delay epoch, neurons in the ALM showed selective persistent activity (**Figures S2A–S2C**), and unilateral inactivation of the ALM biased future licking to the ipsilateral direction (**Figures S1E–S1H**), confirming that the delay activity in ALM is required for motor planning (**Guo et al., 2014b; Li et al., 2015**). Notably, unilateral inactivation of the ALM significantly reduced performance in contralateral trials and increased performance in ipsilateral trials (**Figures S1F**), in contrast to a general reduction of performance. This pattern of behavioral deficit is consistent with the general organization of cortex, in that the motor and sensory effects of a lesion are usually on the converse side.

We first tested the involvement of the CBTC circuit in STM with temporally precise optogenetic perturbation (**Deisseroth, 2015**). Because SNr efferents target the thalamus as well as multiple brainstem areas, including the superior colliculus, the pedunculo-pontine tegmentum, and reticular formation (**McElvain et al., 2021**), we aimed to specifically perturb SNr projections in the thalamus (**Catanese and Jaeger, 2021; Lalive et al., 2018; Morrisette et al., 2019**). To do so, we injected Cre-recombinase-dependent channelrhodopsin-2 (ChR2) virus in the left SNr of Gad2-IRES-Cre transgenic mice and implanted an optical fiber targeting the left VM (**Figures 1C, 1D, S2D, and S2F; Method details**). Unilateral activation of SNr terminals in the VM during the sample or delay epoch significantly decreased performance for contra-trials (*t* test, $p < 0.001$; **Figures 1E**, power 5 mW, and **S1J**, power 2 mW, 10 mW). The SNr-to-VM projections are GABAergic and the VM-to-ALM projections are glutamatergic. Thus, activation of SNr terminals presumably reduced ALM activity and, subsequently, caused the ipsilateral bias. Notably, activation of SNr projections did not affect lick-early rate, no-response rate, or licking rate (**Figures 1F and S1K–S1L**). Activation during the response epoch had little effect on performance, suggesting that this pathway is not specific for licking execution (**Figure 1E**).

Because activation of SNr terminals can potentially evoke antidromic spikes that complicate the interpretation of behavioral effects, we optogenetically inactivated the SNr terminals in the VM (**Figures 1G and 1H**). To do so, we injected Cre-recombinase-dependent Arch virus in the left SNr of Gad2-IRES-Cre mice and implanted an optical fiber targeting the VM (**Figures S2E and S2F; Method details**). Unilateral inactivation of SNr terminals in the VM during the sample or delay epoch significantly decreased performance for ipsi-trials, producing an opposite behavioral deficit compared with that of the optogenetic activation (*t* test, $p < 0.001$ or 0.01 ; **Figures 1I**, laser power 20 mW, **S1M**, and **S1N**, laser power 5 mW, 10 mW). The opposite effects, caused by activation and inactivation perturbations, indicated that behavioral deficits were not caused by heating of

neural tissue (**Owen et al., 2019**). Inactivation also produced a small increase in performance for contra-trials (the effect reached significance when combining trials from different laser powers; **Figure S1N**). Similar to activation, inactivation during the delay epoch did not affect the lick-early rate, no-response rate, and licking rate (**Figures 1J, S1O, and S1P**). Inactivation during the response epoch had a small effect on performance ($8\% \pm 1\%$ for contra-trials; $-7\% \pm 6\%$ for ipsi-trials; means \pm SEM; **Figure 1I**), but that effect was not consistently observed at different laser powers (**Figure S1N**). These results suggest that the basal ganglia-to-thalamus pathway is critical for STM.

The basal ganglia-to-thalamus pathway differentially modulates cortical activity

To check whether activation of SNr terminals ubiquitously reduced the activity of ALM neurons, we simultaneously recorded single-units from the ALM (**Figures 2 and S3A–S3G**). We identified 705 single-units from the left ALM ($n = 7$ mice) and focused on putative pyramidal neurons ($n = 467/705$; **Figures S2A–S2C; Method details**). Activation of SNr terminals during the delay epoch did not uniformly reduce the ALM activity (mean firing rate significantly changed, 11.2% up, 16.1% down, *t* test, $p < 0.05$, **Figures 2B–2D**; see **Figures S3A–S3G** for activity during sample epoch activation). Interestingly, neurons with different response properties were differentially modulated (**Figure 2D**). For contra-preferring neurons, there were significantly more down-modulated than up-modulated neurons (17.1% versus 6.7%, chi-square test, $p < 0.05$). For ipsi-preferring neurons, there were significantly more up-modulated than down-modulated neurons (19.7% versus 7.6%, $p < 0.05$; **Figure 2D**). The pattern of modulation, quantified as the ratio of up-modulated neurons, was significantly different between contra- and ipsi-preferring neurons (chi-square test, $p < 0.01$; **Method details**). The differential effect on contra- and ipsi-preferring neurons was caused by the preferential shift of activity in contra-trials to ipsi-trials (example neurons in **Figure 2B** and averaged activity in **Figures 2E and 2F**). Overall, activation of SNr terminals only slightly reduced ALM mean activity but significantly reduced selectivity (defined as the absolute difference of activity in contra- and ipsi-trials; selectivity reduction, $39.3\% \pm 12.1\%$ during the last 300 ms of the delay epoch, means \pm SEM, *t* test, $p < 0.001$; mean activity reduction $6.6\% \pm 4.7\%$; **Figure 2G**). To understand the diverse effect on individual neurons in ALM, we examined simultaneously recorded population activity in high-dimensional space (**Figure 2H**). Population activity evolved with trial progression to form a trajectory in contra- or ipsi-trials. We then performed dimensionality reduction by projecting trajectories along the coding direction (CD, along which activity maximally discriminated upcoming directional licking) (**Li et al., 2016**). Activation of SNr terminals pushed the projected contra-trajectory toward the ipsi-trajectory and left the ipsi-trajectory relatively unchanged (**Figure 2H**). There were similar fraction of neurons modulated by SNr activation in ipsi- and contra-trials (14.2% versus 15.7%, *t* test, $p = 0.6$). However, the change of activity in contra- rather than ipsi- trials had a much larger component along the CD, resulting in the specific modulation of the contra-trajectory (**Figure 2H**).

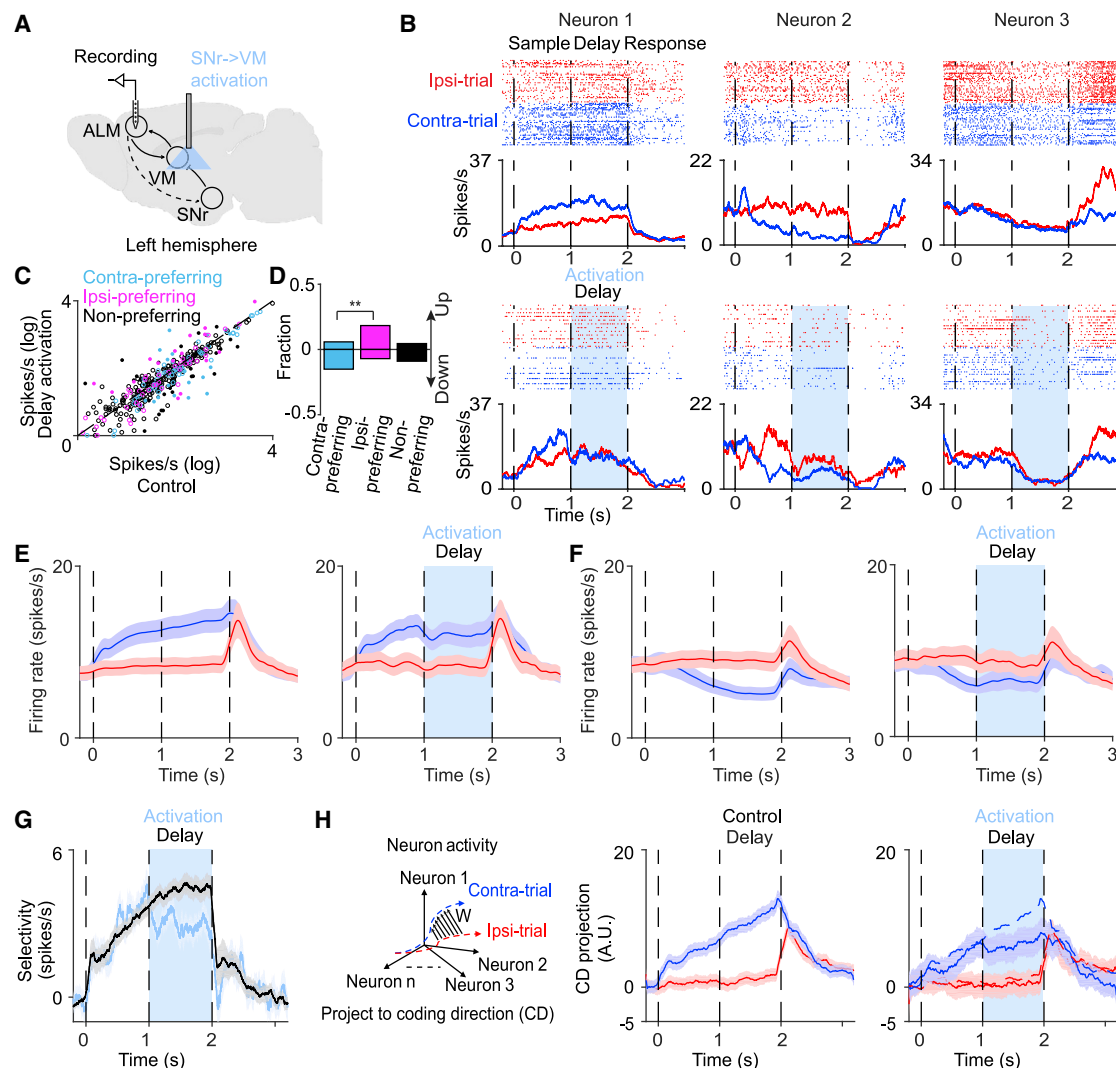


Figure 2. Activation of SNr-to-thalamus axons selectively modulates ALM activity

(A) Schematic of recording in ALM during optogenetic activation of SNr axons near the VM.

(B) Three example ALM neurons during the SNr terminal activation. Top: spike raster and peri-stimulus time histogram (PSTH). Bottom: spike raster and PSTH during SNr terminal activation. Correct contra- (blue) and ipsi- (red) trials only. Dashed lines separate behavioral epochs. Bin size, 1 ms. Averaging window, 100 ms.

(C) Scatterplot of mean firing rates during the delay epoch (428 units with at least 6 activation trials from 7 mice). Cyan, contra-preferring neurons; magenta, ipsi-preferring neurons; black, non-preferring neurons; filled circles, neurons that are significantly modulated ($p < 0.05$, t test). Dotted line is the unity line.

(D) Fraction of up- and down-modulated neurons in each group shown in (C). ** $p < 0.01$, chi-square test.

(E) Mean PSTH of ALM contra-preferring neurons ($n = 86$ neurons) during control (left panel) and SNr terminal activation (right panel). Shading, SEM.

(F) Mean PSTH of ALM ipsi-preferring neurons ($n = 71$ neurons) during control (left panel) and SNr terminal activation (right panel). Shading, SEM.

(G) Selectivity of ALM neurons during control (black) and SNr terminal activation (blue). Shading, SEM.

(H) Activation of SNr terminals biased neural trajectory in contra-trials toward that in the ipsi-trials. Left, schematic of neuronal activity space. Blue and red curves indicate the population trajectory in the contra- and ipsi-trials, respectively. W, coding direction (CD); middle and right, CD projected activity during control (middle) and SNr terminal activation (right). Shading, SEM ($n = 7$ mice). Bin size, 10 ms. Averaging window, 10 ms.

See also Figure S3.

We inferred that, by tuning down the inhibitory modulation from the SNr, the ipsi-trajectory should move toward the contra-trajectory. To test that, we recorded single-units from the ALM during inactivation of SNr terminals (Figures 3A and 3B). Inactivation, compared with activation, produced the opposite modulation patterns of ALM activity, consistent with oppo-

site behavioral deficits (Figures 3C, 3D, S3J, S3K, and S3P). The differential effect on contra- and ipsi-preferring neurons was caused by the preferential shift of activity in ipsi-trials to that in contra-trials (example neurons in Figure 3B and averaged activity in Figures 3E and 3F). Inactivation on average increased ALM activity by $36.2\% \pm 6.7\%$ but dramatically reduced ALM

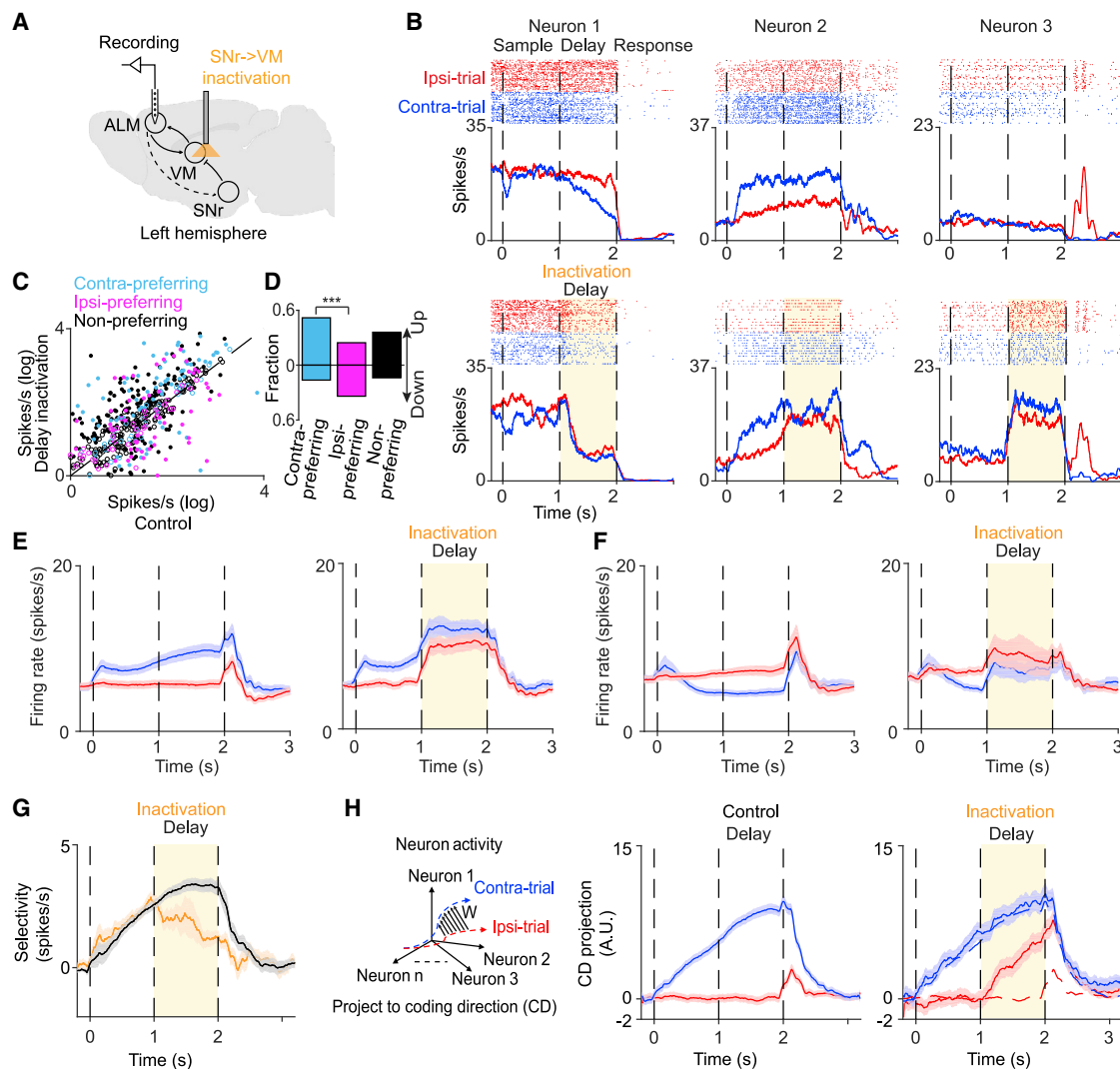


Figure 3. Inactivation of SNr-to-thalamus axons selectively modulates ALM activity

(A) Recording in ALM during inactivation of SNr-to-VM axons.

(B) Three examples of ALM neurons during SNr terminal inactivation. Top: spike raster and PSTH. Bottom: spike raster and PSTH during SNr terminal inactivation. Correct contra- (blue) and ipsi- (red) trials only. Dashed lines separate behavioral epochs. Bin size, 1 ms. Averaging window, 100 ms.

(C) Scatterplot of mean firing rates during the delay epoch (577 neurons with at least 6 inactivation trials from 10 mice). Cyan, contra-prefering neurons; magenta, ipsi-prefering neurons; black, non-prefering neurons; filled circles, neurons that are significantly modulated ($p < 0.05$, t test). Dotted line is the unity line.

(D) Fraction of up-modulated neurons and down-modulated neurons in each group shown in (C). *** $p < 0.001$, chi-square test.

(E) Mean PSTH of ALM contra-prefering neurons ($n = 110$ neurons) during control (left panel) and SNr terminal inactivation (right panel). Shading, SEM.

(F) Mean PSTH of ALM ipsi-prefering neurons ($n = 106$ neurons) during control (left panel) and SNr terminal inactivation (right panel). Shading, SEM.

(G) Selectivity of ALM neurons during control (black) and SNr terminal inactivation (orange). Shading, SEM.

(H) Inactivation of SNr terminals biased neural trajectory in ipsi-trials toward that in contra-trials. Left, schematic of neuronal activity space. Middle and right, CD projected activity during control (middle) and SNr terminal inactivation (right). Same format as in Figure 2H. Shading, SEM ($n = 10$ mice).

See also Figure S3 and S5.

selectivity ($63.7\% \pm 9.8\%$ reduction, means \pm SEM, t test, $p < 0.001$; Figure 3G). Inactivation of SNr terminals preferentially affected the projected ipsi-trajectory without changing the contra-trajectory (Figure 3H). Thus, with reduced SNr activity, the ipsi-trajectory was pushed toward the contra-trajectory, consistent with our hypothesis (Figure 3H).

Inactivation of the SNr-to-thalamus pathway in the left hemisphere produced a contralateral bias (Figure 3H). The result

was also consistent with a shift of trajectory in lick-left to lick-right trials. To differentiate the two possibilities, we inactivated SNr terminals in the right hemisphere (Figures S4A). Inactivation produced a slight contralateral bias (Figure S4D) and, consequently, biased trajectories in the direction from ipsi- to contra-trajectory (the trajectory in lick-right trials to that in lick-left trials; Figure S4I). Thus, inactivation in both hemispheres caused a contralateral bias relative to the perturbed side. However, we

also found that the bias in behavior and neural trajectory was small during inactivation of the right SNr. Several reasons might underlie the small bias. First, optogenetic inactivation of the right ALM only induced small behavioral deficits in the task (Yin et al., 2019). Second, the interaction in the right CBTC circuit might be weaker because the right hemisphere seemed to have a less-dominant role in behavior (Yin et al., 2019).

SNr modulates thalamic activity

To understand how SNr modulated ALM activity through the thalamus, we characterized the effect of SNr inactivation on thalamic activity. An optrode implanted into the thalamus near the VM and VAL served to both inactivate SNr terminals and record thalamic activity. We identified 570 single-units from the left thalamus (6 mice; Figures S2G–S2J and S5). Thalamic neurons showed selectivity during the sample, delay, or response epochs between the contra- and ipsi-trials (Figures S2I and S5B). Inactivation of SNr terminals, on average, only slightly elevated mean thalamic activity by $17.5\% \pm 6.4\%$, but almost completely removed thalamic selectivity (reduction, $100.5\% \pm 11.3\%$ in the sample epoch, $80.3\% \pm 12.2\%$ in the delay epoch; Figures S5D and S5E). Similarly, weak perturbation of the thalamus effectively reduced ALM selectivity (Guo et al., 2017). Inactivation of SNr terminals pushed the ipsi-trajectory to the contra-trajectory for thalamic neurons (Figure S5F), similar to the effect on ALM activity (Figure 3H). Thus, SNr inactivation shifted the ipsi-trajectory in ALM through its specific effect on thalamic neural trajectory.

SNr activity encodes STM

Perturbation of SNr-to-VM projections modulated the ALM neural trajectory in a trial-type-specific way, suggesting that SNr neurons carry selective information. Because there might exist different functional domains in the SNr (Alexander et al., 1990), we aimed to survey neuronal response properties across the region. Because the SNr sits deep in the brain, we developed a data collection and analysis pipeline to reconstruct recording locations with high precision (Figure S6). We painted the silicon probe with a thin layer of Dil and applied a brief electric pulse to mark a small lesion near the tip of the probe (Figures 4A and 4B) (Huo et al., 2020). We then imaged the entire mouse brain using a custom-built light-sheet microscope (Zhang et al., 2021) and mapped the electrode tracks as well as the lesion location to the common coordinate framework (CCFv3; <http://atlas.brain-map.org/>) (Wang et al., 2020). In total, we recorded 695 single-units from 20 mice performing the STM task. We focused on putative GABAergic neurons ($n = 585/695$), selected based on their narrow spike waveforms (Figures S2K; Method details). This classification was verified by optogenetic tagging of GABAergic neurons (Figures S2L–S2O; Method details). Activity in a majority of neurons differed across trial types (69.2% , $405/585$; $p < 0.01$, Mann-Whitney U test; Method details). Selectivity for future movements emerged in the sample epoch and increased throughout the delay epoch (Figures 4C–4E and S7). Neural responses in the SNr were diverse: subsets of neurons showed selective sample and/or delay activity ($123/585$), perimovement activity during the response epoch ($113/585$), or both ($99/585$; Figure 4E). Similar response types were observed

in the SNr during memory-guided oculomotor planning (Hikosaka and Wurtz, 1983). Approximately equal numbers of neurons preferred contra- or ipsi-lateral movements (Figures 4D and 4E). We also noted that there were more contra-preferring neurons in the sample epoch, possibly because of the stronger tactile stimulus in contra-trials. Consistent with that, the contra-preference in these neurons did not change in error trials (i.e., the neurons were sensory related; Figures S7G and S7H).

Our recording covered most of the SNr (along dorsal-ventral, middle-lateral, and anterior-posterior axes; Figure 4F). Selective neurons were distributed widely in the SNr but with a hotspot located in the mediolateral region (Figures 4F, S6C, and S6D). Neurons within the hotspot had significantly greater selectivity (Figure 4G). Retrograde labeling from the VM, one major ALM projection zone in the thalamus, showed that VM-projecting SNr neurons were also widely distributed but seemed to concentrate in the mediolateral part (Guo et al., 2017). These results suggest that this region of the SNr is primarily involved in regulation of ALM activity, revealing one channel linking SNr-VM-ALM for STM (Alexander et al., 1990).

We further characterized how well SNr neurons encoded task information. For each neuron, a set of trials was randomly selected with equal proportions of lick-left correct, lick-left error, lick-right correct, and lick-right error trials. Activity of individual neurons predicted the strength of whisker stimulation (strong or weak), choice (lick the left or right spout), and outcome (correct or incorrect response) with variable accuracy (characterized by area under receiver operating characteristic curve [AUC]; Figures 5A–5C). For prediction of sensory stimulus, activity in the sample, rather than in the delay epoch performed better (Figure 5A). For prediction of choice, activity in the delay or response, rather than in the sample epoch, performed better (Figure 5B). We then randomly selected a pseudo-population of neurons and trained a support vector machine (SVM) classifier with 10-fold cross-validation (see Method details). The classifier reached high accuracy ($\sim 85\%$) with 200 randomly selected neurons (Figure 5D). We then randomly selected 200 neurons to examine how the decoding accuracy of sensory, choice, and outcome evolved with trial progression. Sensory information was greatest at the early sample epoch, whereas choice information gradually increased from sample to delay and reached the peak at the beginning of the response epoch (Figures 5E and 5F). Consistently, outcome information only emerged in the response epoch (Figure 5G). Notably, SNr neurons performed similarly or even better than ALM neurons (Figures S8M–S8P). These results indicate that trial information can be decoded from SNr activity with high accuracy.

Do selective neurons in SNr have greater correlation? To check this, we characterized the noise correlation (NC) between pairs of simultaneously recorded neurons. NC reflects shared input as well as functional connectivity between pairs of neurons (Cohen and Kohn, 2011). Many neuron pairs had high NCs compared with shuffled trials (Figure 5H). NCs positively correlated with signal correlation (Figure 5I). Interestingly, contra- and ipsi-preferring neurons, compared with non-preferring neurons, showed significantly greater NCs, and the difference disappeared with trials shuffled (Figures 5J and 5K). Notably, contra- and ipsi-preferring neurons were anti-correlated. These

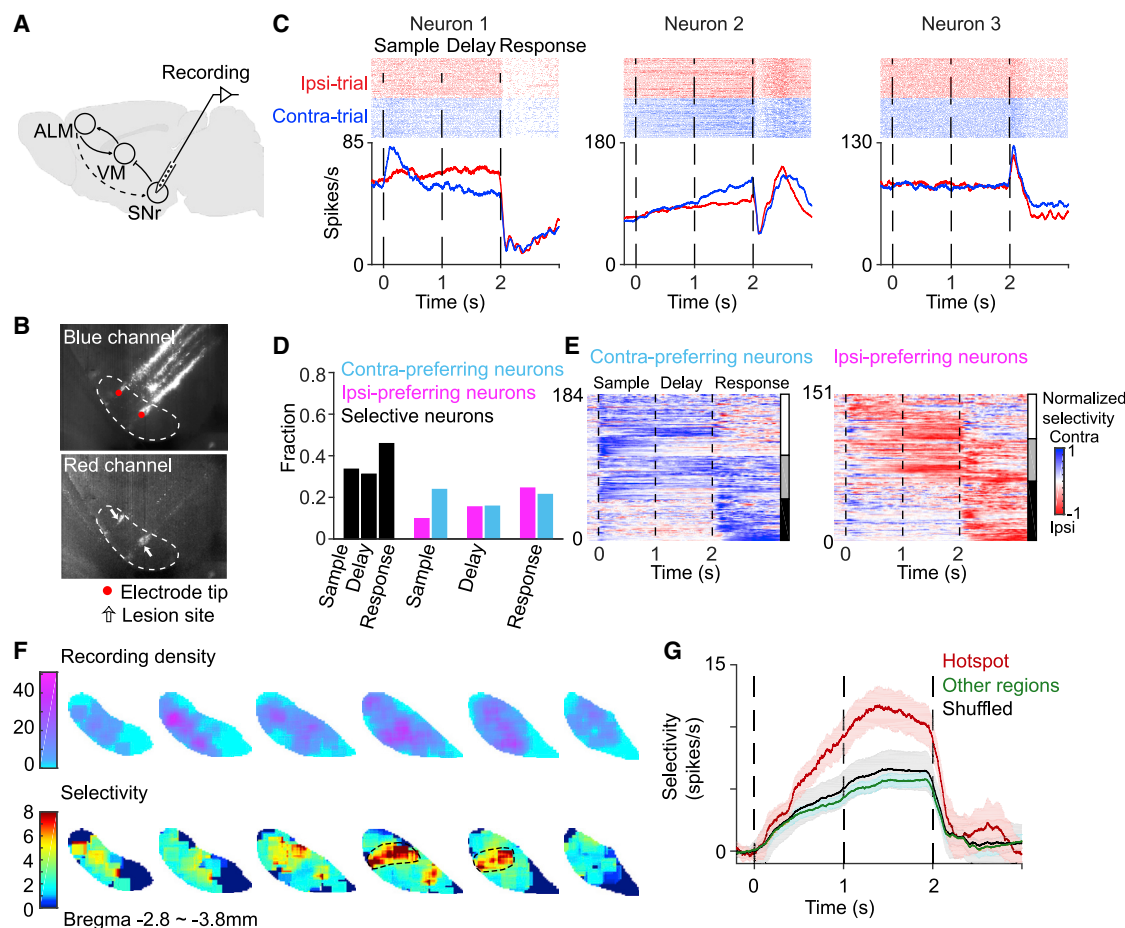


Figure 4. Recording throughout SNr reveals a selectivity hotspot

(A) Schematic of silicon probe recording in SNr.

(B) Reconstruction of recording locations. Fluorescence image showing electrode tracks, lesion sites, and the mapped tips of the recording probe (four shanks) aligned to the Allen Reference Atlas.

(C) Three example SNr neurons. Top: spike raster. Bottom: PSTH of contra- (blue) and ipsi- (red) trials. Dashed lines separate behavioral epochs (as in Figure 2B). Bin size, 1 ms. Averaging window, 100 ms.

(D) Fraction of selective SNr neurons in the sample, delay, or response epoch.

(E) SNr population selectivity ($n = 335$). Vertical bars on the right: white, neurons with preparatory activity only; gray, neurons with both preparatory activity and peri-movement activity; black, neurons with peri-movement activity only. Units that switched preference in different epochs were excluded.

(F) Distribution of recording density and selectivity in SNr (see Method details). Dotted line, outline of the hotspot with higher selectivity.

(G) Selectivity in the hotspot (red) and the rest (green) of the SNr. Black, spatial positions shuffled. Shading, SEM.

See also Figure S6.

results suggest that SNr neurons with similar selectivity have greater trial-to-trial co-fluctuations.

SNr selectivity depends on ALM

Does trial-type information in the SNr depend on the ALM? To answer that, we simultaneously recorded SNr activity during ALM inactivation (Figure 6A). Inactivation during the delay epoch dramatically reduced selectivity in SNr neurons (t test, $p < 0.001$; Figures 6B and 6G; see Figures S7A–S7F for sample epoch inactivation) but, on average, only slightly reduced SNr activity (3.4 ± 1.4 spikes, $-9.7\% \pm 3.7\%$ of delay epoch activity, means \pm SEM). This reduction of selectivity was observed for all response types of SNr neurons; selectivity in neurons differentiating sample,

delay, or response epochs were equally reduced ($p > 0.5$, t test). Inactivation did not uniformly modulate SNr activity either (mean firing rate, 8.2% up, 32.6% down, 59.3% unchanged during delay epoch inactivation; Figures 6C and 6D; similar fraction during sample epoch inactivation; Figure S7C). Neurons with different response preferences were differentially modulated. For contra-preferring neurons, there were more down-modulated than up-modulated neurons (51.5% versus 7.8%, $p < 0.001$, chi-square test; Figure 6D). For ipsi-preferring neurons, there were similar fractions of up-modulated and down-modulated neurons (26.5% versus 23.5%; Figure 6D). The pattern of modulation in contra-preferring neurons was significantly different from that in ipsi-preferring neurons (chi-square test, $p < 0.001$). The difference

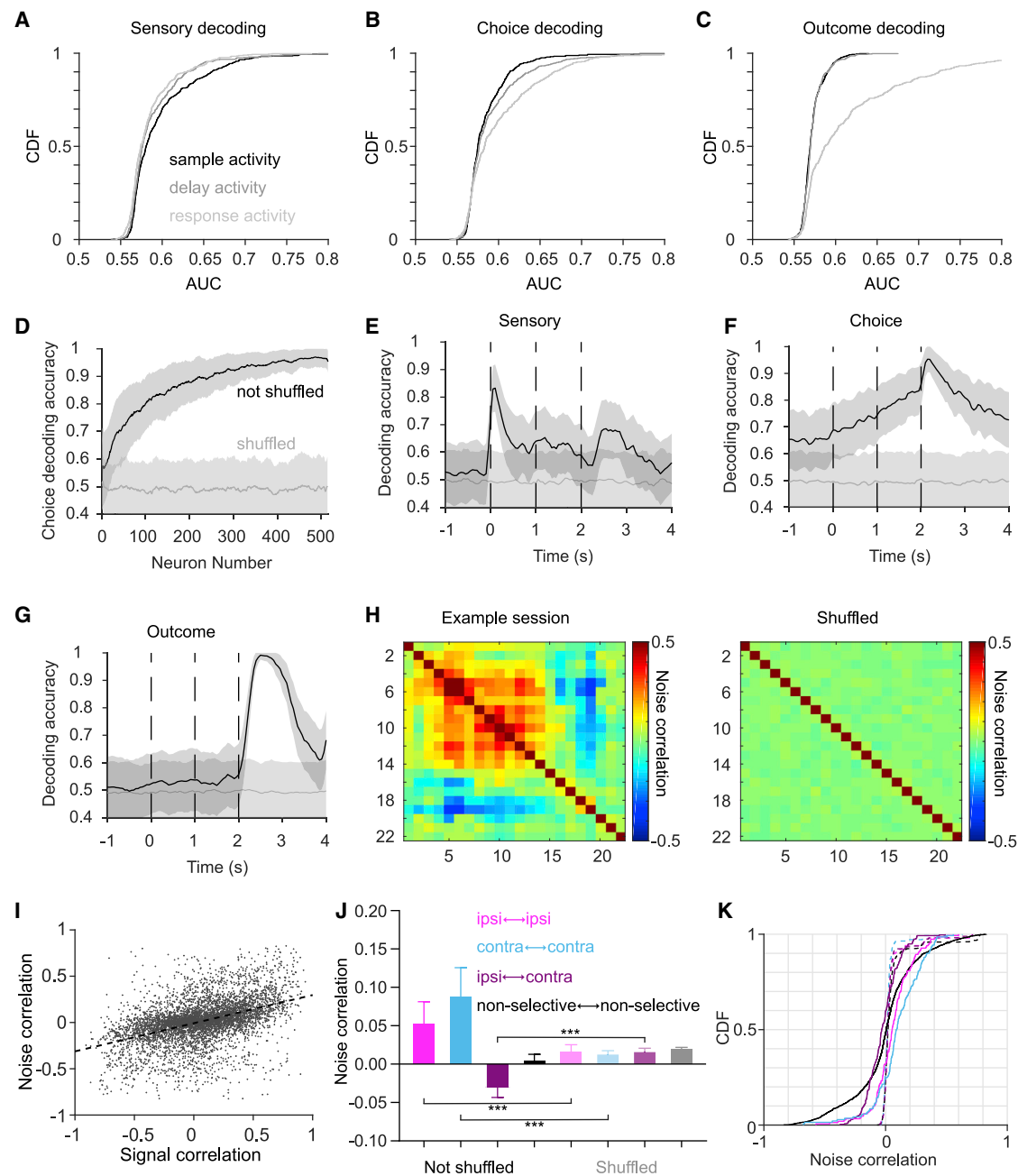


Figure 5. SNr neurons encode sensory, choice, and outcome information

(A) Decoding of sensory information (i.e., weak and strong whisker stimuli associated with lick-left and lick-right trials, respectively) by individual neurons. Accuracy is quantified by the area under the ROC curve (AUC). ROC, receiver operating characteristic; CDF, cumulative distribution function. The sample epoch activity (black) decodes better than the delay activity does (gray).

(B) Similar to (A) but for the decoding of choice.

(C) Similar to (A) but for the decoding of outcome (correct versus incorrect response).

(D) The accuracy of choice decoded using a support vector machine (SVM) classifier increases with the number of neurons (see [Method details](#)). Light line, control with trial labels shuffled; shading, standard deviation.

(E) The decoding accuracy of sensory information along trial progression based on 200 randomly selected neurons with balanced trial types (see [Method details](#)). Light line, control with trial labels shuffled; shading, standard deviation.

(F) The decoding accuracy of choice. Same format as in (E).

(G) The decoding accuracy of outcome. Same format as in (E).

(H) Noise correlations of simultaneously recorded neurons in an example session. Trial labels are shuffled in the right panel.

(I) Relationship between the noise correlation and signal correlation (see [Method details](#)). Each dot represents a pair of neurons.

(legend continued on next page)

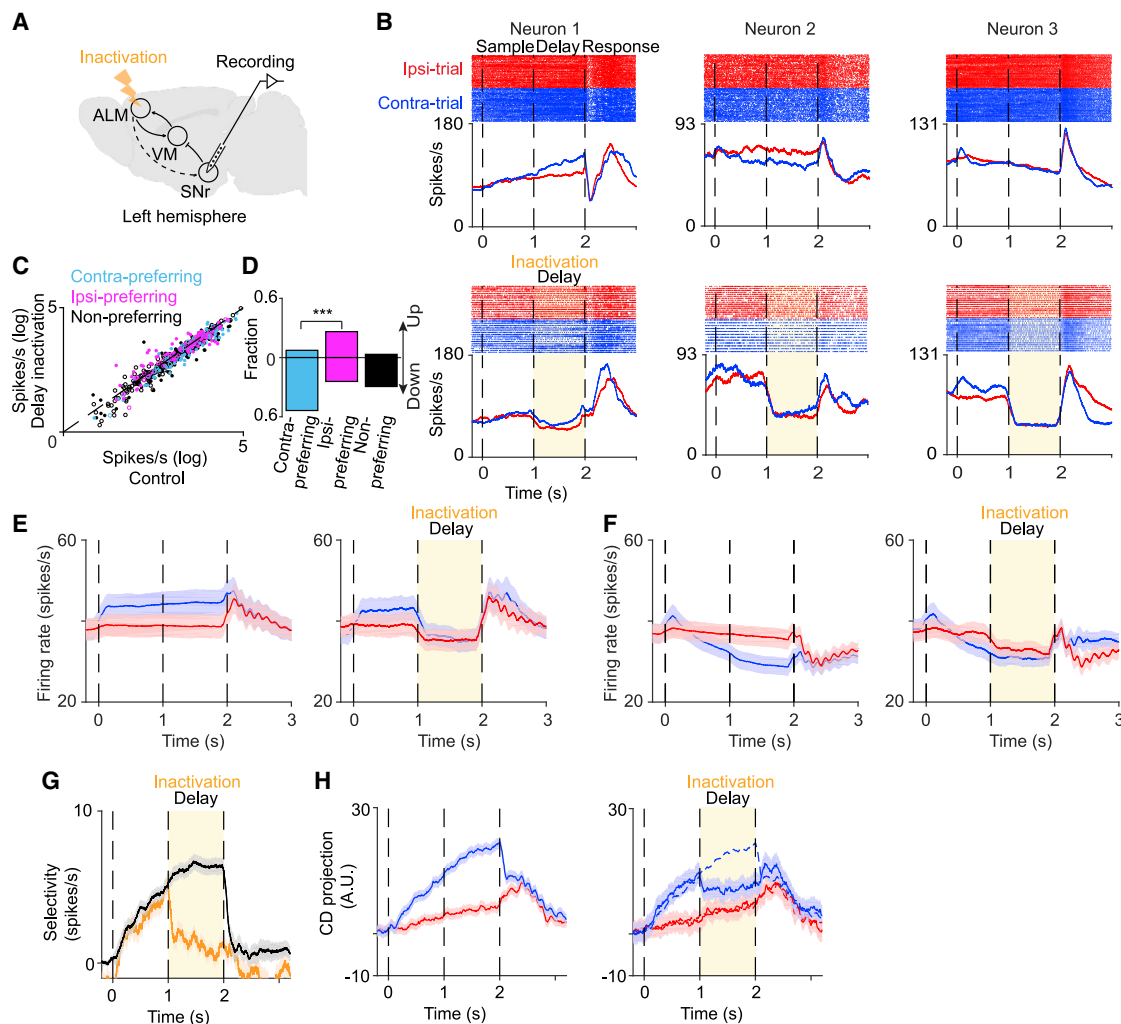


Figure 6. Inactivation of ALM selectively modulates SNr activity

(A) Recording in SNr during ALM inactivation.
(B) Three example SNr neurons during ALM inactivation. Top: spike raster and PSTH. Bottom: spike raster and PSTH during ALM inactivation. Correct contra- (blue) and ipsi- (red) trials only. Dashed lines separate behavioral epochs. Bin size, 1 ms. Averaging window, 100 ms.
(C) Scatterplot of mean firing rates during the delay epoch (585 neurons from 20 mice). Same format as in Figure 2C.
(D) Fraction of up-modulated neurons and down-modulated neurons in each group shown in (C). *** $p < 0.001$, chi-square test.
(E) Mean PSTH of the SNr contra-prefering neurons ($n = 95$ neurons) during control (left) and ALM inactivation (right). Shading, SEM.
(F) Mean PSTH of the SNr ipsi-prefering neurons ($n = 95$ neurons) during control (left) and ALM inactivation (right). Shading, SEM.
(G) Selectivity of SNr neurons during control (black) and ALM inactivation (orange). Shading, SEM.
(H) Coding direction-projected activity during control (left) and ALM inactivation (right). Inactivation of ALM biased contra-trajectory toward the ipsi-trajectory. Dotted lines, trajectories in control trials (from the left). Shading, SEM ($n = 20$ mice). Bin size, 10 ms. Averaging window, 10 ms.
See also Figure S7.

was due to the differential effect of cortical inactivation on SNr neurons; mean activity in contra-prefering neurons in both contra- and ipsi-trials was reduced whereas mean activity in ipsi-prefering neurons was differentially modulated (Figures 6E and 6F). Exam-

ination of SNr activity along the coding direction showed that inactivation pushed the contra-trajectory toward ipsi-trajectory and left the ipsi-trajectory relatively unchanged (Figure 6H). This suggests that ALM provides trial-type specific information to SNr.

(J) Ipsi-prefering (magenta) and contra-prefering (cyan) neurons have significantly greater noise correlations than non-prefering (dark) and shuffled neurons. Ipsi-prefering and contra-prefering neurons are anti-correlated. Whisker, median with 95% confidence interval; *** $p < 0.001$, bootstrap.

(K) CDF of noise correlation in different groups of neurons. The color scheme is the same as in (J). Solid lines, data not shuffled. Dotted lines, data shuffled. See also Figure S8.

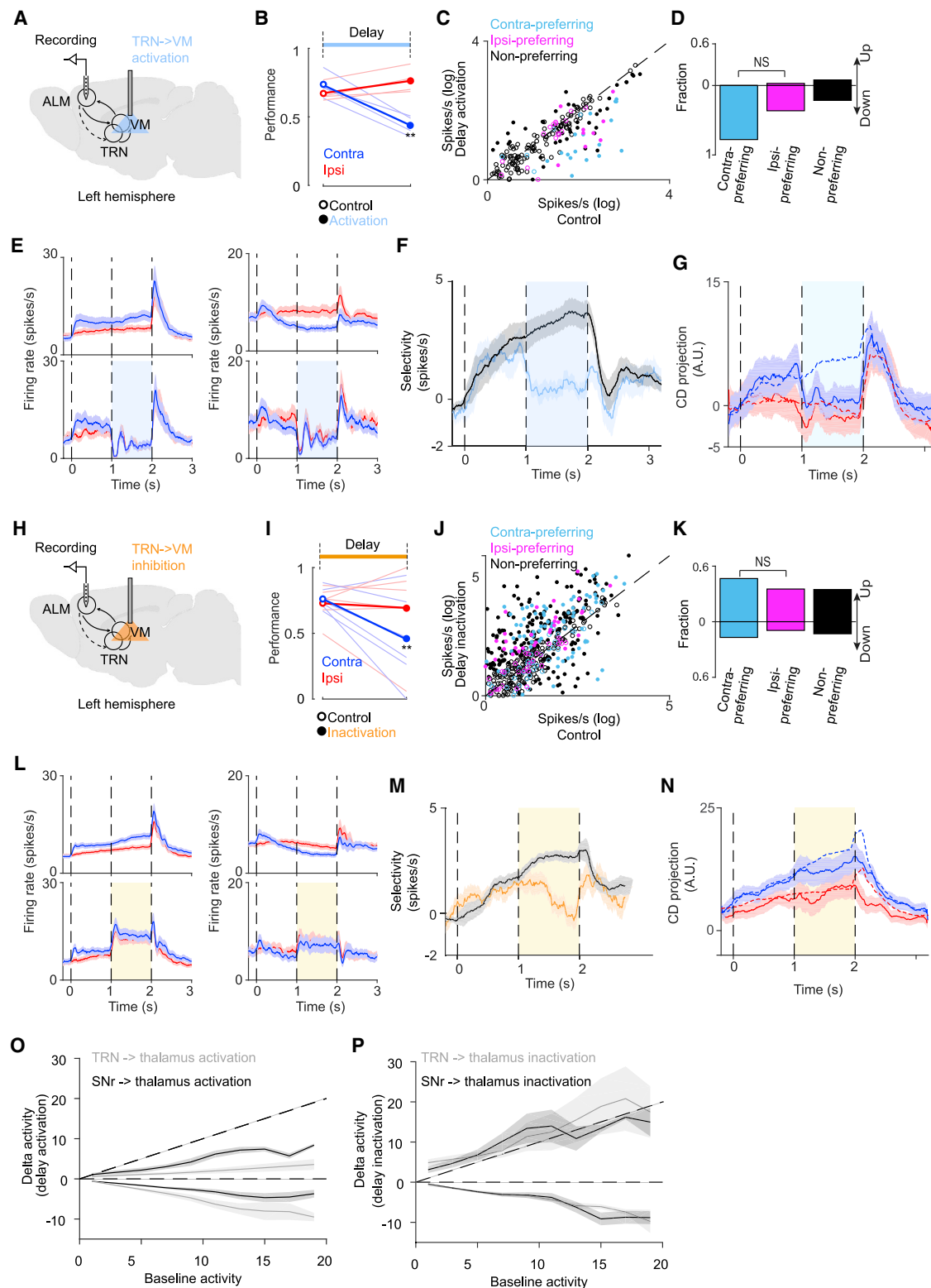


Figure 7. TRN-to-thalamus pathway modulates ALM activity differently from SNr-to-thalamus pathway

(A) Schematic of recording in the ALM during optogenetic activation of the TRN terminals near the VM, relevant to (B)–(G).

(B) Optogenetic activation of TRN terminals during the delay epoch produces an ipsilateral bias ($n = 4$ mice). Each line represents a mouse (Method details). $^{**}p < 0.01$, t test.

(legend continued on next page)

We wonder how specific the ALM-SNr-VM-ALM circuit is for STM? In addition to strong projections in the VM and VA motor thalamus, SNr neurons also target the mediodorsal (MD) thalamus (McElvain et al., 2021), and the MD strongly activates the medial prefrontal cortex (mPFC) neurons (Collins et al., 2018). To check whether the mPFC is also involved in the CBTC circuit for STM, we optogenetically inactivated the mPFC using the same laser power and transgenic mouse line as in the ALM inactivation (Figure S8). Unilateral inactivation of mPFC did not affect task performance, whereas inactivation of the ALM caused an evident ipsilateral bias (Figures S1E–S1H and S8B). Neurons near mPFC also differentiated trial types in sample, delay, or response epochs (Figures S8E and S8F), but the fraction of selective neurons was significantly smaller than that of ALM neurons (76/735 versus 218/577, $p < 0.001$, chi-square test; Figure S8D). The difference between contra- and ipsi-trajectory along the CD was also significantly smaller (1.5 ± 0.5 vs. 7.7 ± 0.2 , bootstrap, $p < 0.001$; Figure S8H). We further compared the encoding capability of mPFC and ALM neurons (Figures S8I–S8P). Neurons in mPFC encoded choice information significantly worse compared with ALM neurons ($p < 0.05$, t test, Figures S8I–S8P). These results indicate that mPFC is not causally involved in the task and that ALM-SNr-VM-ALM represents an at least partly closed CBTC loop for STM.

Comparison between SNr and thalamic reticular nucleus

The motor thalamus receives major inhibitory inputs from the SNr and the thalamic reticular nucleus (TRN) (Guo et al., 2017; Kuramoto et al., 2011; McElvain et al., 2021). Unilateral inactivation of motor thalamus by stimulating TRN axons impaired performance by creating an ipsilateral bias (Guo et al., 2017), similar to the behavioral deficit after stimulation of the SNr terminals (Figure 2). Does the TRN have a similar role as the SNr in modulating ALM activity to form selective persistent activity? To check that, we recorded ALM activity during optogenetic perturbation of TRN axons (Figure 7). To specifically perturb the motor thalamus-targeting TRN axons, we used Gad2-IRES-Cre mice and injected virus into the motor sector of the TRN that was previously, retrogradely labeled from the VM (Guo et al., 2017). Cre-recombinase

allowed expression of the optogenetic activator or silencer in TRN neurons targeting the motor thalamus. Three pieces of evidence indicated that the TRN affected ALM activity differently from that of the SNr. First, both activation and inactivation of TRN projections caused an ipsilateral bias (Figures 7B and 7I). In contrast, activation and inactivation of SNr projections produced the opposite behavioral deficits (Figure 1). Second, activation of TRN uniformly reduced ALM activity in contra-, ipsi-, and non-preferring neurons (Figures 7C–7E). Similarly, inactivation nearly uniformly elevated ALM activity in different response types of neurons (Figures 7J–7L). For comparison, SNr perturbation differentially modulated ALM activity in contra- and ipsi-preferring neurons (Figures 2C–2F and 3C–3F). Third, both activation and inactivation of TRN terminals shifted contra-trajectory toward ipsi-trajectory (Figures 7G and 7N), whereas perturbation of SNr projections differentially biased neural trajectories (Figures 2 and 3). The difference is unlikely to be due to saturation of ALM activity during TRN perturbations. First, the shift of the neural trajectory was consistent with the behavioral bias in both TRN and SNr perturbations (Figures 2H, 3H, 7G, and 7N). Second, the change of ALM activity (i.e., delta activity) had a similar relationship with the baseline activity during TRN and SNr perturbations (Figures 7O and 7P). The slope was shallower during TRN activation, compared with SNr activation, for the group of positive delta activities, whereas it was steeper for the group of negative delta activities (Figure 7O). For inactivation, the relationship was identical between TRN and SNr (Figure 7P). These results suggest that the ALM-SNr-VM-ALM channel specifically modulates ALM persistent activity to support STM.

DISCUSSION

The basal ganglia have a crucial role in learning, action selection, and movement initiation (Buhusi and Meck, 2005; Catanese and Jaeger, 2021; Graybiel, 2008; Kravitz et al., 2010; Mink, 2003; Yin and Knowlton, 2006). We demonstrated that optogenetic perturbation of the SNr-to-thalamus pathway at the strength that does not affect movement execution can affect cognitive function (Figure 1). Activation or inactivation of SNr axon terminals differentially modulated ALM neurons (depending on their

(C) Scatterplot of mean firing rates during the delay epoch ($n = 284$ neurons). Same format as in Figure 2C.

(D) Fraction of up-modulated neurons and down-modulated neurons in each group. Activity in contra-, ipsi-, and non-preferring neurons is reduced. Same format as in Figure 2D.

(E) Mean PSTH of ALM contra-preferring neurons (left, $n = 27$ neurons) and ipsi-preferring neurons (right, $n = 33$ neurons) during control (top) and optogenetic activation of TRN terminals (bottom). Shading, SEM. Bin size, 1 ms. Averaging window, 100 ms.

(F) Selectivity of ALM neurons during control (black) and activation (blue). Shading, SEM.

(G) Projections along the coding direction during control (dotted) and activation (solid lines). $n = 4$ mice. Shading, SEM. Bin size, 10 ms. Averaging window, 20 ms.

(H) Schematic of recording in the ALM during inactivation of TRN terminals near the VM, relevant to (H)–(N).

(I) Optogenetic inactivation of TRN terminals during the delay epoch produces an ipsilateral bias ($n = 6$ mice). Each line represents a mouse (Method details). *** $p < 0.001$, t test.

(J) Scatterplot of mean firing rates during the delay epoch ($n = 709$ neurons). Same format as in Figure 2C.

(K) Fraction of up-modulated neurons and down-modulated neurons in each group. Activity in each group is increased. Same format as in Figure 2D.

(L) Mean PSTH of ALM contra-preferring neurons (left, $n = 121$ neurons) and ipsi-preferring neurons (right, $n = 85$ neurons) during control (top) and optogenetic inactivation of TRN terminals (bottom). Shading, SEM.

(M) Selectivity of ALM neurons during control (black) and inactivation (orange). Shading, SEM.

(N) Projections along the coding direction during control (dotted) and inactivation (solid lines). $n = 6$ mice. Shading, SEM. Bin size, 10 ms. Averaging window, 20 ms.

(O) Change of ALM activity during TRN (gray) or SNr (black) terminal activation. Activity change was separated into the positive and negative groups. Dotted, unity line. Shading, SEM.

(P) Change of ALM activity during TRN (gray) or SNr (black) terminal inactivation. Shading, SEM.

response types), resulting in a specific shift of neural trajectories in the ALM (Figures 2 and 3). That specific effect is achieved through selective regulation of neural trajectories in the thalamus (Figure S5). Similarly, inactivation of ALM selectively affected neural trajectories in the SNr (Figure 6). These results demonstrate that the CBTC circuit is crucial for the formation of trial-type-specific persistent activity underlying STM. For comparison, another inhibitory source to thalamus, the reticular nucleus, does not specifically regulate cortical activity (Figure 7). It is shown that discrete attractor dynamics in the ALM underlie STM, with an external input help to push attractors to discrete endpoints that predict different choices (Inagaki et al., 2019). SNr perturbations only weakly modulated thalamic activity. However, this weak modulation strongly reduced ALM selectivity, indicating that nonlinear amplification is involved in the circuit. The basal ganglia possibly function through the thalamus as an external input to modulate ALM activity to form discrete attractors.

Selectivity of SNr neurons is widely distributed, but there is a hotspot centered in the mediolateral part with much greater selectivity (Figure 4). SNr selectivity depends on ALM activity (Figure 6). Another pathway involving SNr-MD-mPFC is not necessary for the task (Figure S8). Thus, a closed loop involving ALM-SNr-VM-ALM is crucial for ALM activity to form specific neural trajectories encoding discrete licking choices. Anatomical and physiological findings indicate that the CBTC pathways form distinct parallel streams through different sectors of the cerebral cortex, basal ganglia, and thalamus (Alexander et al., 1990). The motor loops are involved in the control of movement speed, direction, and amplitude of body, eye, and limbs, whereas the non-motor loops function to modulate the expression of cognitive and affective behavior. Given the anatomical similarity of non-motor loops to the relatively better-understood motor loops, functions of motor loops might shed light on the non-motor regulatory functions. Both Parkinson and Huntington diseases, which are caused by the dysfunction of the basal ganglia system, adversely affect diverse cognitive functions, including working memory, selective attention, and planning (Bosboom et al., 2004), indicating that the SNr-to-thalamus pathway might be generally involved in cognition. Consistently, the SNr also projects broadly in the medial dorsal thalamus, which is involved in selective attention and working memory (Bolkan et al., 2017; Schmitt et al., 2017).

It is after learning that neurons in the ALM show persistent activity that predicts future licking directions. The basal ganglia are crucial for the association of different sensory cues with reward outcomes through learning. Perturbing the SNr-to-thalamus pathway shifts neural trajectory specifically in ipsi-trials (inactivation) or contra-trials (activation). Activation or inactivation of the TRN-to-thalamus pathway perturbs neural activity similarly in contra- and ipsi-trials, in contrast to the differential effect caused by SNr terminal perturbations. The difference between SNr and TRN highlights the importance of the basal ganglia system in specifically regulating cortical activity. How the CBTC circuit shapes its connectivity through learning to support different neural trajectories remains to be elucidated. Persistent activity is widely observed in various cortical and subcortical areas (Curtis and Lee, 2010; Erlich et al., 2011; Funahashi et al., 1989; Fuster and Alexander, 1971; Gao et al., 2018; Guo et al., 2014b, 2017;

Hanks et al., 2015; Hikosaka and Wurtz, 1983; Kopec et al., 2015; Romo et al., 1999; Tanji and Evarts, 1976). In ALM, persistent activity depends on the thalamocortical reciprocal projections with VM (Guo et al., 2017), is disrupted by stimulation of the vestigial nucleus of cerebellum (Gao et al., 2018) and can be regulated by the contralateral ALM (Li et al., 2016; Yin et al., 2019). How a multi-regional network, involving ALM, basal ganglia, cerebellum, thalamus, and other modulatory inputs, coordinates persistent activity to form selective trajectories underlying different STM requires further investigation.

STAR★METHODS

Detailed methods are provided in the online version of this paper and include the following:

- **KEY RESOURCES TABLE**
- **RESOURCE AVAILABILITY**
 - Lead contact
 - Materials availability
 - Data and code availability
- **EXPERIMENTAL MODEL AND SUBJECT DETAILS**
 - Mice
- **METHOD DETAILS**
 - Surgery
 - Virus injection
 - Behavior
 - Histology
 - Reconstruction of silicon probe locations in SNr
 - Inactivation of ALM or mPFC
 - Perturbation of SNr-to-VM or TRN-to-VM terminals
 - Extracellular electrophysiology
- **QUANTIFICATION AND STATISTICAL ANALYSIS**
 - Behavioral data analysis
 - Electrophysiology data analysis
 - Decoding of sensory, choice and outcome information
 - Optical tagging of SNr GABAergic neurons
 - Statistics

SUPPLEMENTAL INFORMATION

Supplemental information can be found online at <https://doi.org/10.1016/j.neuron.2021.08.002>.

ACKNOWLEDGMENTS

We thank Chunyu Duan, Zhenyu Gao, Hidehiko Inagaki, Jorge Jaramillo, Nuo Li, Karel Svoboda, and Ning-long Xu for comments on the manuscript and the animal core facility at Tsinghua University for maintaining the mouse lines. This work was supported by the National Natural Science Foundation of China (31871048, 32021002).

AUTHOR CONTRIBUTIONS

Y.W., Z.Z., J.L., and W.Z. performed the experiments. Y.W., X.Y., J.L., and W.Z. analyzed the data. Y.W., X.Y., and Z.V.G. conceived the project. Y.W., X.Y., and Z.V.G. wrote the paper with comments from other authors.

DECLARATION OF INTERESTS

The authors declare no competing interests.

Received: April 20, 2020
Revised: June 26, 2021
Accepted: August 3, 2021
Published: August 31, 2021

REFERENCES

- Alexander, G.E., Crutcher, M.D., and DeLong, M.R. (1990). Basal ganglia-thalamocortical circuits: parallel substrates for motor, oculomotor, "prefrontal" and "limbic" functions. *Prog. Brain Res.* 85, 119–146.
- Avants, B.B., Tustison, N., and Song, G. (2009). Advanced normalization tools (ANTS). *Insight J.* 2, 1–35.
- Bolkan, S.S., Stujenske, J.M., Parnaudeau, S., Spellman, T.J., Rauffenbart, C., Abbas, A.I., Harris, A.Z., Gordon, J.A., and Kellendonk, C. (2017). Thalamic projections sustain prefrontal activity during working memory maintenance. *Nat. Neurosci.* 20, 987–996.
- Bosboom, J.L., Stoffers, D., and Wolters, E.Ch. (2004). Cognitive dysfunction and dementia in Parkinson's disease. *J. Neural Transm. (Vienna)* 111, 1303–1315.
- Buhusi, C.V., and Meck, W.H. (2005). What makes us tick? functional and neural mechanisms of interval timing. *Nat. Rev. Neurosci.* 6, 755–765.
- Catanese, J., and Jaeger, D. (2021). Premotor ramping of thalamic neuronal activity is modulated by nigral inputs and contributes to control the timing of action release. *J. Neurosci.* 41, 1878–1891.
- Chow, B.Y., Han, X., Dobry, A.S., Qian, X., Chuong, A.S., Li, M., Henninger, M.A., Belfort, G.M., Lin, Y., Monahan, P.E., and Boyden, E.S. (2010). High-performance genetically targetable optical neural silencing by light-driven proton pumps. *Nature* 463, 98–102.
- Christophel, T.B., Klink, P.C., Spitzer, B., Roelfsema, P.R., and Haynes, J.D. (2017). The distributed nature of working memory. *Trends Cogn. Sci.* 21, 111–124.
- Cohen, M.R., and Kohn, A. (2011). Measuring and interpreting neuronal correlations. *Nat. Neurosci.* 14, 811–819.
- Collins, D.P., Anastasiades, P.G., Marlin, J.J., and Carter, A.G. (2018). Reciprocal circuits linking the prefrontal cortex with dorsal and ventral thalamic nuclei. *Neuron* 98, 366–379.e4.
- Curtis, C.E., and Lee, D. (2010). Beyond working memory: the role of persistent activity in decision making. *Trends Cogn. Sci.* 14, 216–222.
- Deisseroth, K. (2011). Optogenetics. *Nat. Methods* 8, 26–29.
- Deisseroth, K. (2015). Optogenetics: 10 years of microbial opsins in neuroscience. *Nat. Neurosci.* 18, 1213–1225.
- Dotson, N.M., Hoffman, S.J., Goodell, B., and Gray, C.M. (2018). Feature-based visual short-term memory is widely distributed and hierarchically organized. *Neuron* 99, 215–226.e4.
- Erich, J.C., Bialek, M., and Brody, C.D. (2011). A cortical substrate for memory-guided orienting in the rat. *Neuron* 72, 330–343.
- Funahashi, S., Bruce, C.J., and Goldman-Rakic, P.S. (1989). Mnemonic coding of visual space in the monkey's dorsolateral prefrontal cortex. *J. Neurophysiol.* 61, 331–349.
- Fuster, J.M., and Alexander, G.E. (1971). Neuron activity related to short-term memory. *Science* 173, 652–654.
- Gao, Z., Davis, C., Thomas, A.M., Economo, M.N., Abrego, A.M., Svoboda, K., De Zeeuw, C.I., and Li, N. (2018). A cortico-cerebellar loop for motor planning. *Nature* 563, 113–116.
- Gold, J.I., and Shadlen, M.N. (2007). The neural basis of decision making. *Annu. Rev. Neurosci.* 30, 535–574.
- Graybiel, A.M. (2008). Habits, rituals, and the evaluative brain. *Annu. Rev. Neurosci.* 31, 359–387.
- Guo, Z.V., Hires, S.A., Li, N., O'Connor, D.H., Komiyama, T., Ophir, E., Huber, D., Bonardi, C., Morandell, K., Gutnisky, D., et al. (2014a). Procedures for behavioral experiments in head-fixed mice. *PLoS ONE* 9, e88678.
- Guo, Z.V., Li, N., Huber, D., Ophir, E., Gutnisky, D., Ting, J.T., Feng, G., and Svoboda, K. (2014b). Flow of cortical activity underlying a tactile decision in mice. *Neuron* 81, 179–194.
- Guo, Z.V., Inagaki, H.K., Daie, K., Druckmann, S., Gerfen, C.R., and Svoboda, K. (2017). Maintenance of persistent activity in a frontal thalamocortical loop. *Nature* 545, 181–186.
- Hanks, T.D., Kopec, C.D., Brunton, B.W., Duan, C.A., Erlich, J.C., and Brody, C.D. (2015). Distinct relationships of parietal and prefrontal cortices to evidence accumulation. *Nature* 520, 220–223.
- Hikosaka, O., and Wurtz, R.H. (1983). Visual and oculomotor functions of monkey substantia nigra pars reticulata. III. Memory-contingent visual and saccade responses. *J. Neurophysiol.* 49, 1268–1284.
- Hippenmeyer, S., Vrieseling, E., Sigrist, M., Portmann, T., Laengle, C., Ladle, D.R., and Arber, S. (2005). A developmental switch in the response of DRG neurons to ETS transcription factor signaling. *PLoS Biol.* 3, e159.
- Huo, Y., Chen, H., and Guo, Z.V. (2020). Mapping functional connectivity from the dorsal cortex to the thalamus. *Neuron* 107, 1080–1094.e5.
- Inagaki, H.K., Inagaki, M., Romani, S., and Svoboda, K. (2018). Low-dimensional and monotonic preparatory activity in mouse anterior lateral motor cortex. *J. Neurosci.* 38, 4163–4185.
- Inagaki, H.K., Fontolan, L., Romani, S., and Svoboda, K. (2019). Discrete attractor dynamics underlies persistent activity in the frontal cortex. *Nature* 566, 212–217.
- Jun, J.J., Mitelut, C., Lai, C., Gratiy, S.L., Anastasiades, C.A., and Harris, T.D. (2017). Real-time spike sorting platform for high-density extracellular probes with ground-truth validation and drift correction. *BioRxiv*.
- Kopec, C.D., Erlich, J.C., Brunton, B.W., Deisseroth, K., and Brody, C.D. (2015). Cortical and subcortical contributions to short-term memory for orienting movements. *Neuron* 88, 367–377.
- Kravitz, A.V., Freeze, B.S., Parker, P.R., Kay, K., Thwin, M.T., Deisseroth, K., and Kreitzer, A.C. (2010). Regulation of parkinsonian motor behaviours by optogenetic control of basal ganglia circuitry. *Nature* 466, 622–626.
- Kuramoto, E., Fujiyama, F., Nakamura, K.C., Tanaka, Y., Hioki, H., and Kaneko, T. (2011). Complementary distribution of glutamatergic cerebellar and GABAergic basal ganglia afferents to the rat motor thalamic nuclei. *Eur. J. Neurosci.* 33, 95–109.
- Laliv, A.L., Lien, A.D., Roseberry, T.K., Donahue, C.H., and Kreitzer, A.C. (2018). Motor thalamus supports striatum-driven reinforcement. *eLife* 7, e34032.
- Li, N., Chen, T.W., Guo, Z.V., Gerfen, C.R., and Svoboda, K. (2015). A motor cortex circuit for motor planning and movement. *Nature* 519, 51–56.
- Li, N., Daie, K., Svoboda, K., and Druckmann, S. (2016). Robust neuronal dynamics in premotor cortex during motor planning. *Nature* 532, 459–464.
- Li, N., Chen, S., Guo, Z.V., Chen, H., Huo, Y., Inagaki, H.K., Chen, G., Davis, C., Hansel, D., Guo, C., and Svoboda, K. (2019). Spatiotemporal constraints on optogenetic inactivation in cortical circuits. *eLife* 8, e48622.
- Liu, D., Gu, X., Zhu, J., Zhang, X., Han, Z., Yan, W., Cheng, Q., Hao, J., Fan, H., Hou, R., et al. (2014). Medial prefrontal activity during delay period contributes to learning of a working memory task. *Science* 346, 458–463.
- McElvain, L.E., Chen, Y., Moore, J.D., Brigidi, G.S., Bloodgood, B.L., Lim, B.K., Costa, R.M., and Kleinfeld, D. (2021). Specific populations of basal ganglia output neurons target distinct brain stem areas while collateralizing throughout the diencephalon. *Neuron* 109, 1721–1738.e4.
- Mink, J.W. (2003). The Basal Ganglia and involuntary movements: impaired inhibition of competing motor patterns. *Arch. Neurol.* 60, 1365–1368.
- Morrisette, A.E., Chen, P.H., Bhamani, C., Borden, P.Y., Waiblinger, C., Stanley, G.B., and Jaeger, D. (2019). Unilateral optogenetic inhibition and excitation of basal ganglia output affect directional lick choices and movement initiation in mice. *Neuroscience* 423, 55–65.
- Murakami, M., Vicente, M.I., Costa, G.M., and Mainen, Z.F. (2014). Neural antecedents of self-initiated actions in secondary motor cortex. *Nat. Neurosci.* 17, 1574–1582.

- Owen, S.F., Liu, M.H., and Kreitzer, A.C. (2019). Thermal constraints on in vivo optogenetic manipulations. *Nat. Neurosci.* 22, 1061–1065.
- Pan, C., Cai, R., Quacquarelli, F.P., Ghasemigharagoz, A., Loubopoulos, A., Matryba, P., Plesnila, N., Dichgans, M., Hellal, F., and Ertürk, A. (2016). Shrinkage-mediated imaging of entire organs and organisms using uDISCO. *Nat. Methods* 13, 859–867.
- Pinto, L., Rajan, K., DePasquale, B., Thiberge, S.Y., Tank, D.W., and Brody, C.D. (2019). Task-dependent changes in the large-scale dynamics and necessity of cortical regions. *Neuron* 104, 810–824.e9.
- Romo, R., Brody, C.D., Hernández, A., and Lemus, L. (1999). Neuronal correlates of parametric working memory in the prefrontal cortex. *Nature* 399, 470–473.
- Schmitt, L.I., Wimmer, R.D., Nakajima, M., Happ, M., Mofakham, S., and Halassa, M.M. (2017). Thalamic amplification of cortical connectivity sustains attentional control. *Nature* 545, 219–223.
- Siegle, J.H., López, A.C., Patel, Y.A., Abramov, K., Ohayon, S., and Voigts, J. (2017). Open Ephys: an open-source, plugin-based platform for multichannel electrophysiology. *J. Neural Eng.* 14, 045003.
- Stringer, C., Pachitariu, M., Steinmetz, N., Reddy, C.B., Carandini, M., and Harris, K.D. (2019). Spontaneous behaviors drive multidimensional, brainwide activity. *Science* 364, 255.
- Svoboda, K., and Li, N. (2018). Neural mechanisms of movement planning: motor cortex and beyond. *Curr. Opin. Neurobiol.* 49, 33–41.
- Taniguchi, H., He, M., Wu, P., Kim, S., Paik, R., Sugino, K., Kvitsiani, D., Fu, Y., Lu, J., Lin, Y., et al. (2011). A resource of Cre driver lines for genetic targeting of GABAergic neurons in cerebral cortex. *Neuron* 71, 995–1013.
- Tanji, J., and Evarts, E.V. (1976). Anticipatory activity of motor cortex neurons in relation to direction of an intended movement. *J. Neurophysiol.* 39, 1062–1068.
- Wang, Q., Ding, S.L., Li, Y., Royall, J., Feng, D., Lesnar, P., Graddis, N., Naeemi, M., Facer, B., Ho, A., et al. (2020). The allen mouse brain common coordinate framework: a 3D reference atlas. *Cell* 181, 936–953.e20.
- Yin, H.H., and Knowlton, B.J. (2006). The role of the basal ganglia in habit formation. *Nat. Rev. Neurosci.* 7, 464–476.
- Yin, X., Wang, Y., Li, J., and Guo, Z.V. (2019). Experience-dependent hemispheric dominance during motor planning. *Neuron*. Published online December 27, 2019. <https://doi.org/10.2139/ssrn.3510215>.
- Zhang, Z., Yao, X., Yin, X., Ding, Z., Huang, T., Huo, Y., Ji, R., Peng, H., and Guo, Z.V. (2021). Multi-scale light-sheet fluorescence microscopy for fast whole brain imaging. *Frontiers In Neuroanatomy* 15, 732464.

STAR★METHODS

KEY RESOURCES TABLE

REAGENT or RESOURCE	SOURCE	IDENTIFIER
Bacterial and virus strains		
AAV9-EF1a-DIO-eArch3.0-EYFP	Vigenebio	N/A
AAV9-EF1a-DIO-hChR2(H134R)-mCherry	Vigenebio	N/A
Chemicals, peptides, and recombinant proteins		
Dil	Invitrogen	D282; CAS: 41085-99-8
CellTracker CM-Dil Dye	Invitrogen	C7001; CAS: 180854-97-1
Experimental models: Organisms/strains		
Mouse: Rosa26 CAG-LSL-ReaChR-mCit	The Jackson Laboratory	Stock No. 026294
Mouse: PV-Cre	The Jackson Laboratory	Stock No. 008069
Mouse: Gad2-IRES-Cre	The Jackson Laboratory	Stock No. 010802
Software and algorithms		
MATLAB 2017b & 2018a	MathWorks	https://www.mathworks.com/products/matlab.html ; RRID: SCR_001622
LabVIEW	National Instruments	https://www.ni.com/enus/shop/labview.html ; RRID: SCR_014325
SpikeGL	Janelia Research Campus	https://github.com/cculianu/SpikeGL
SpikeGLX	Janelia Research Campus	https://billkarsh.github.io/SpikeGLX
Kilosort2	Stringer et al., 2019	https://github.com/MouseLand/Kilosort2
JRCLUST	Jun et al., 2017	https://github.com/JaneliaSciComp/JRCLUST
ZEN Digital Imaging for Light Microscopy	Zeiss	https://www.zeiss.com/microscopy/int/products/microscope-software/zen.html ; RRID: SCR_013672
Other		
473 nm laser	Chang Chun Optics	MBL-FN-473-300 mW
594 nm laser	Obis LS, Coherent	OBIS 594-100 mW
	Chang Chun Optics	MGL-N-593.5 nm-200 mW
Acousto-optical modulator	Quanta Tech	MTS110-A3-VIS
64-channel silicon probes	Cambridge NeuroTech	ACUTE-64-4-250 probe
NeuroPixels probes	Imec	NeuroPixels 1.0
Scanning galvo	Thorlabs	GVS012
Fully Automated Vibrating Blade Microtome	Leica	VT1200S
Source data	This paper; Mendeley Data	https://dx.doi.org/10.17632/4wrnxhxxjf.1

RESOURCE AVAILABILITY

Lead contact

Further information and requests for resources and reagents should be directed to and will be fulfilled by the lead contact, Zengcai V. Guo (guozengcai@tsinghua.edu.cn).

Materials availability

This study did not generate new unique reagents.

Data and code availability

- The behavior and electrophysiology data generated during this study are available at Mendeley Data (<https://dx.doi.org/10.17632/4wrnxhxxjf.1>).
- The MATLAB code used to produce main results of this study is available at Mendeley Data (<https://dx.doi.org/10.17632/4wrnxhxxjf.1>).

- Any additional information required to reanalyze the data reported in this paper is available from the lead contact upon request.

EXPERIMENTAL MODEL AND SUBJECT DETAILS

Mice

This study is based on data from 122 mice (age > P60, male). Fifty-two mice were used for training only and seventy were used for experiments with optogenetic perturbation and/or recording. PV-Cre (JAX 008069) (Hippenmeyer et al., 2005) × R26-CAG-LSL-ReaChR-mCitrine (JAX 026294) (Li et al., 2019) transgenic mice were used for ALM inactivation and SNr recording experiments (22 mice) and mPFC inactivation experiments (4 mice). Gad2-IRES-Cre (JAX 010802) (Taniguchi et al., 2011) transgenic mice were used for SNr-to-VM optogenetic inactivation (16 mice) or activation (12 mice), characterization of inactivation effects on thalamic activity (6 mice), and TRN-to-VM optogenetic inactivation (6 mice) or activation (4 mice). All experimental procedures were approved by the Institutional Animal Care and Use Committee at Tsinghua University, Beijing, China. Mice were housed with siblings to allow social contact. A 12:12 reverse light: dark cycle was used and behavioral tests were done during the dark phase.

METHOD DETAILS

Surgery

All surgical procedures were carried out aseptically under 1.5%–2% isoflurane anesthesia. Flunixin meglumine (Sichuan Dingjian Animal Medicine Co., Ltd) was injected subcutaneously (1.25 mg/kg) during and after the surgery for at least three days to reduce inflammation.

Mice were prepared for electrophysiology and photostimulation with a head-bar and a clear-skull cap (Guo et al., 2014b). The scalp of the mouse was removed to expose the skull covering the dorsal cortex. After clearing the exposed cranium, a thin layer of cyanoacrylate adhesive (Krazy glue, Elmer's Products Inc) was directly applied to the intact skull. A custom titanium bar was glued to the skull (approximately over the cerebellum). Two holes were drilled over cerebellum and two silver pins (Digi-Key Part Number, ED90488-ND) were inserted into the holes as ground and reference during electrophysiology. Dental acrylic (Lang Dental Jet Repair Acrylic; Part# 1223-clear) was applied to fix the head bar. To allow light efficiently passing through, the dental acrylic was polished and covered by a thin layer of clear nail polish (Electron Microscopy Sciences, Part# 72180).

For SNr or TRN terminal perturbation, an optical fiber was implanted above VM (AP −1.5, ML 0.75, DV 3.9 mm). For mPFC inactivation, an optical fiber at 15° was implanted above PrL (AP 1.7, ML 0.7, DV 1.7–2.0 mm). For extracellular recording in ALM, thalamus or SNr, a small craniotomy (~2–3 mm square) was made to allow electrode to penetrate through the dura. After craniotomy or recording, the exposed brain was covered by artificial dura and silica gel for protection (Guo et al., 2014b).

Virus injection

AAV9-EF1a-DIO-eArch3.0-EYFP virus (Vigenebio, Shandong) or AAV9-EF1a-DIO-hChR2(H134R)-mCherry virus (Vigenebio, Shandong) was injected in SNr or TRN of Gad2-IRES-Cre mice to specifically label GABAergic neurons for optogenetic inactivation and activation experiments (Chow et al., 2010; Deisseroth, 2011). Injection was targeted to SNr (AP −3.0, ML 1.5, DV 4.65 mm) using a volumetric injection system (modified from Mo-10 Narishige). In total, three mice were injected 300 nL of eArch3.0 virus and thirteen mice were injected 100 nL eArch3.0 as we found this amount of virus was sufficient to infect most parts of SNr or TRN. For characterization of inactivation effects on thalamic neurons, four mice were injected 100 nL of eArch3.0 virus. For activation experiments, twelve mice were injected 100 nL ChR2 virus. The injection rate was about 10 nL/min. Mice injected with different amount of eArch3.0 virus showed similar behavior and electrophysiological results and the data were pooled together.

Behavior

The behavioral training was modified from before (Guo et al., 2014a). A metal pole, attached to the shaft of a mirror galvanometer (with the attached mirror removed), was presented near the right side of whiskers of mice (~6 mm away from the base of whiskers). A two-spout lickport was used to record licking events and deliver milk as rewards. During each trial, the pole was controlled by the galvanometer to vibrate at 10 Hz in order to simulate natural whisker stimulation. The strength of the stimulus was adjusted by changing the current input to the galvanometer (~1800 °/s peak velocity for the strong stimulus and ~400 °/s peak velocity for the weak stimulus). For the strong stimulus, mice were trained to lick right (contralateral to the recorded left hemisphere) while for the weak stimulus mice need to lick left (ipsilateral to the recorded left hemisphere) in order to obtain reward. The stimulus lasted for one second in the sample period, followed by a one second delay period. Then an auditory go cue (0.1 s) separated the delay and the response period. Correct licking during response period resulted in a reward (~4 μL milk). Licking during the sample or delay period (lick-early trials) would cause a timeout (1 s). Licking the incorrect lickport (error trials) or not licking within 1 s after the go cue (no-response trials) would lead to end this trial and start the next trial. These lick-early and no-response trials were excluded from analyses of performance and neural activity (Figures 1, 2, 3, 4, 5, 6, and 7).

Each behavioral session lasted for ~1.5–2 hours with ~600–800 trials. After each training session, mice were supplied additional 1.5–3 g solid food (depending on the performance of the mouse on that day) to maintain a stable body weight (> 85% of the weight before training).

Histology

Mice were perfused transcardially with PBS followed by 4% PFA. The brains were fixed in 4% PFA overnight then sectioned into slices (70 μm /slice) by a vibratome (VT1200 S, Leica). Images were acquired by a slide scanner microscope (Zeiss Axio Scan.Z1, 10 \times objective). Electrode tracks labeled with Dil were used to determine recording locations. Tissue damage caused by optical fiber insertion was used to determine inactivation locations (Figure S2). One mouse brain was severely deformed during this processing (third from the left in Figure S2D) and the fiber tip could only be accurately determined to be about 1 mm away from VM.

Reconstruction of silicon probe locations in SNr

For recordings in SNr, we used whole brain imaging to locate recording sites. To label recording tracks, the probe was painted with a thin layer of CM-Dil (Invitrogen, dissolved in Ethanol, Beijing chemical works) before recording. Before withdrawing the probe, a small current (20 μA , 1 s, 4–6 times) was delivered to produce a lesion near the tip of the probe. After the last session of recording, the animal was perfused and the brain was fixed with 4% PFA overnight. The fixed brain was washed with PBS three times. Bone debris and hairs were removed from the surface of the brain. Then the brain was cleared with uDISCO (Pan et al., 2016). The cleared brain was imaged with a customized light-sheet microscope at $3 \times 3 \times 8 \mu\text{m}^3$ resolution (Figure S6). Images from the blue channel (488 nm excitation) was used to manually segment CM-Dil signal. Images from the red channel (647 nm excitation) was used to register the imaged brain to the common coordinate framework (CCF; <http://atlas.brain-map.org/>). Images were first down-sampled to $25 \times 25 \times 25 \mu\text{m}^3$ resolution and then aligned to the CCF using advanced normalization tools (ANTs) (Avants et al., 2009). First, an affine transformation was performed to correct translation, shift, stretch and rotation. Then, a b-spline transformation was used to adjust non-rigid inconformity. The deformation field from the red channel was then applied to the blue channel which allowed us to align the brain together with the probe track and lesion locations to the CCF. In total, we recorded 1399 neurons near SNr and located 695 neurons in SNr (Figures 4, 5, and S6). Recording density was defined as the number of recorded neurons within 100 μm^3 (Figures 4F and S6D).

Inactivation of ALM or mPFC

PV-Cre \times R26-CAG-LSLReaChR-mCitrine transgenic mice were used for ALM and mPFC inactivation. Inactivation was deployed randomly on 25% of trials. To prevent mice from distinguishing inactivation trials with control trials by visual cues, a LED pulse train was delivered near the eyes of the mice (i.e., ‘masking flash’, 40 \times 1 ms pulses at 10 Hz, Luxeon Star). The masking flash began 1 s before the start of a trial and ended when the trial finished.

Orange light from a 594 nm laser (Chang Chun optics; Obis LS, Coherent) was controlled by an acousto-optic modulator (AOM; MTS110-A3-VIS, Quanta Tech; extinction ratio 1:2000) to produce a sinusoidal temporal profile with 1.5 mW averaged power. A mechanical shutter (Uniblitz LS6S2T0, Vincent Associates) was used to block light completely for non-inactivation periods. For ALM inactivation, a 2D scanning galvo system (GVS012, Thorlabs) was used to deliver light to the left ALM (AP 2.5, ML 1.5 mm). For mPFC inactivation, light was delivered with a 100 μm diameter optical fiber (NA = 0.22; Thorlabs or Inper) to reach PrL. Laser lasted for 1 s on sample, delay or response epoch (including a 100ms ramping down period to reduce activity rebound). In total, 22 mice were tested for ALM inactivation, 4 mice were tested for mPFC inactivation.

Perturbation of SNr-to-VM or TRN-to-VM terminals

Light was delivered with a 100 μm diameter optical fiber (NA = 0.22; Thorlabs or Inper) to reach VM (AP -1.5 , ML 0.75, DV 3.9 mm) in order to perturb SNr-to-VM or TRN-to-VM terminals. SNr projects strongly to the VM and VA motor thalamus (Kuramoto et al., 2011; McElvain et al., 2021). Although our optical fiber was implanted over VM, optogenetic perturbation might also affect adjacent nuclei including VA and VL.

For activation, we delivered a train of laser pulses (473 nm, 2 ms pulse at 40Hz, Chang Chun Optics). The duration was 1 s for the sample or response epoch and 1.1 s for the delay epoch (an additional 0.1 s covering the cue period to reduce potential rebound activity in the thalamus and ALM). Three laser powers were tested for behavior (peak power 2, 5 and 10 mW; randomly selected in 25% of trials and randomly applied in sample, delay or response epochs) and the 5 mW laser power was further used for electrophysiological experiments. In total, 12 mice were tested for the SNr-to-VM activation experiments and 4 mice were tested for the TRN-to-VM activation experiments.

For inactivation, we used a continuous laser protocol (594 nm, Chang Chun Optics, or Obis LS from Coherent). The duration was 1 s for the sample or response epoch and 1.0 or 1.1 s (including 100 ms linear ramp down) for the delay epoch. Three laser powers were tested for behavioral performance (5, 10 and 20 mW; randomly selected in 25% of trials and randomly applied in sample, delay or response epochs), and the 20 mW laser power was further used for electrophysiological experiments. In total, 16 mice were tested for the SNr-to-VM inactivation experiments (11 of them for behavioral analysis), and 6 mice were tested for the TRN-to-VM inactivation experiments.

Our perturbations caused large behavioral deficits in the delay epoch, slightly smaller deficits in the sample epoch and little deficits in the response epoch (Figures 1, 7, and S1). This suggests that our perturbation operates in the regime mainly affecting sensory perception and STM.

Extracellular electrophysiology

All recordings were made from head-fixed mice. Extracellular spikes were recorded by 64-channel silicon probes (4 shank probes with 250 μ m shank spacing and 12.5 μ m site spacing, Cambridge NeuroTech) or NeuroPixels probes (NeuroPixels 1.0). For recordings using 64-channel probes, the voltage signals were multiplexed, recorded on a USB-6366 board at 400 kHz (National Instrument), and digitalized at 16 bits by custom made headstage (Janelia Farm Research Campus, Brian Barbarits and Tim Harris). The signals were demultiplexed into 64-voltage traces, sampled at 25k Hz and stored by spikeGL (C. Culianu and Anthony Leonardo, Janelia Farm Research Campus). Alternatively, the voltage signals were acquired by an acquisition board (each channel sampled at 25k Hz, OpenEphys; <https://www.open-ephys.org>) (Siegle et al., 2017). Spikes were sorted offline in JRClust (Jun et al., 2017). For recordings using NeuroPixels probes, the voltage signals were acquired through SpikeGLX (Bill Karsh and Tim Harris, Janelia Research Campus.).

PV-Cre \times R26-CAG-LSLReaChR-mCitrine mice were used for SNr recording during ALM inactivation. A small craniotomy (diameter, 2 mm) was made over the contralateral visual cortex (center, bregma AP -3.2 , ML 2.5 mm) or the ipsilateral visual cortex (center, bregma AP -3.2 , ML -3 mm) one day prior to the recording session. A silicon probe was driven down about 6.0 mm at an oblique angle (45° when lowering the probe from the contralateral hemisphere or 15° when lowering the probe from the ipsilateral hemisphere) to reach SNr. There were typically two recording sessions per probe penetration and each session lasted for about 300 trials. Between sessions (lasting for ~ 10 mins), the probe was driven 225 μ m deeper by a micromanipulator (Sutter Instrument). Before withdrawing the probe, a mild current delivered by an electric stimulator (20 μ A, 1 s, 4-6 times, Digitimer DS3, Welwyn Garden City, UK) was used to mark a small lesion at the recording location.

Gad2-IRES-Cre mice were used for recording in ALM, mPFC and VM during perturbations of SNr-to-VM or TRN-to-VM projections. For recordings in ALM or mPFC, a small craniotomy (diameter, 3 mm) was made over the motor cortex (center, bregma AP 2.0 , ML 1.5 or -1.5 mm). The silicon probe was driven down about 0.6-0.8 mm at an oblique angle (15° , i.e., perpendicular to the dura) to record ALM or mPFC neurons. For recordings in the thalamus near VM, a craniotomy (diameter, 3 mm) was made over the dorsal medial somatosensory cortex (center, bregma AP 1.5 , ML 1.8 mm). A silicon optrode (Cambridge NeuroTech) with an optic fiber (100 μ m diameter, 500 μ m away from the electrode tips) was driven down about 4 mm at an oblique angle (15°) to record neurons in VM.

QUANTIFICATION AND STATISTICAL ANALYSIS

Behavioral data analysis

Behavior performance was calculated as the fraction of correct trials, excluding 'lick early' and 'no-response' trials. 'Lick early' rate was the fraction of trials in which mice licked before the response epoch. 'No-response' rate was the fraction of trials in which mice did not lick during the response period. 'Licking rate' was the lick frequency during the response epoch (1 ms bin size, smooth window 200 ms, Figures 1F and 1J). We separately computed the performance for contra- and ipsi-trials relative to the manipulation side (Figures 1 and S1). Behavioral effects of inactivation were quantified by comparing the performance during inactivation with control performance (Figures 1 and S1). Significance of change in performance, 'lick early' rate, 'no-response' rate and 'licking rate' was determined using Student's *t* test.

After trimming whiskers on the right side of the cheek, performance was reduced to change level (Figure S1D). Significance was determined by comparing the performance of the session after trimming whiskers with the previous 10 sessions using Student's *t* test.

Electrophysiology data analysis

For recordings using 64-channel silicon probes, extracellular recording traces were band-filtered (300-6kHz). Events that exceeded an amplitude threshold (4 standard deviations of the background) were sorted using JRClust (Jun et al., 2017). Results from the JRClust were further manually curated through deletion, merging and splitting. For recordings using NeuroPixels probes, we used Kilosort2 to perform clustering (Stringer et al., 2019). Before feeding the data into Kilosort2, we first used CatGT (<https://billkarsh.github.io/SpikeGLX/>) to subtract the averaged value of the signals sampled at the same time to reduce the common noise. Kilosort2 could give many candidate clusters (even up to thousands). We used the pipeline developed by the Allen Institute for Brain Science (ephys_spike_sorting) to select high quality units: 1) removing repeated spikes in each cluster, 2) finding clusters that were likely to be noise, 3) calculating the properties of each cluster and 4) using the quality matrix to select units. Selected units need to meet the following criteria: 1) they were annotated by Kilosort2 as 'Single Unit', 2) they were not annotated as a noise cluster, 3) the average firing rate was higher than 1 Hz, 4) the average amplitude of the waveform was higher than 100 μ V, 5) the estimated time of appearance was higher than 0.8.

We isolated 705 single-units from the left ALM across 46 behavior sessions in 7 mice during activation of SNr-to-VM terminals. Spike width was calculated as the trough-to-peak interval in the mean spike waveform. The distribution of spike widths was bimodal (Figure S2). For recordings using 64-channel silicon probes, units with width < 0.4 ms were defined as putative fast-spiking (FS) neurons and units with width > 0.6 ms as putative pyramidal (PPy) neurons. The classification was previously verified by optogenetic tagging of GABAergic neurons (Guo et al., 2014b). For recordings using NeuroPixels probes, spikes were high-pass filtered, which would reduce the spike width. So neurons with a width < 0.3 were regarded as FS. Neurons with a width > 0.3 and < 0.6 were re-

garded as PPy. We recorded 106/705 FS neurons and 467/705 PPy neurons. We further isolated 693 single units from the left ALM across 44 behavior sessions in 10 mice during inactivation of SNr-to-VM terminals (83 putative fast-spiking neurons, 577 putative pyramidal neurons and 33 unclassified neurons). We focused our analyses on putative pyramidal neurons (Figures 2, 3, S3, and S4).

We isolated 695 single-units from the left SNr across 97 sessions in 20 mice. Units with spike trough-to-peak width < 0.4 ms were selected as putative GABAergic neurons (585/695). These units have high firing rates (35.4 ± 0.4 spikes/s, mean \pm SD). For comparison, neurons with longer spike widths have lower firing rates (28.8 ± 0.2 spikes/s, mean \pm SD, $n = 97/695$; among them only 13/695 with trough-to-peak > 0.6, 10.8 ± 0.4 spikes/s). We focused our analyses on putative GABAergic neurons (Figures 4, 5, 6, S6, and S7).

We isolated 1751 single-units from the left thalamus across 35 behavior sessions in 6 mice. Among these, 1271 single-units were mapped to be within VM/VAL. The distribution of spike widths was bimodal and units with spike width > 0.6 ms were selected as putative thalamic neurons (570/1271). We focused our analyses on putative VM/VAL neurons (Figure S5).

We isolated 924 units from the right ALM during right SNr-to-thalamus inactivation across 23 sessions in 4 mice. Among these, 755 and 169 neurons were classified as PPy neurons and FS neurons respectively (Figure S4).

We isolated 963 units from the left ALM during left TRN-to-thalamus inactivation across 29 sessions in 6 mice. Among these, 761 and 202 neurons were classified as PPy and FS neurons respectively (Figure 7).

We isolated 338 units from the left ALM during left TRN-to-thalamus activation across 16 sessions in 4 mice. Among these, 284 and 54 neurons were classified as PPy neurons and FS neurons respectively (Figure 7).

We recorded 906 units near the left mPFC across 36 sessions in 13 mice. Among these, 735 and 171 neurons were classified as PPy neurons and FS neurons respectively (Figure S8).

Neurons were tested for trial type selectivity during the sample, delay, or response epochs by comparing spike counts during contra- and ipsi-trials (*Mann-Whitney U* test, $p < 0.01$). Neurons that significantly differentiated trial-types during any one of the trial epochs were deemed as “selective”. Neurons with selectivity during the sample or delay epochs were classified as having “preparatory activity.” Neurons with significant selectivity during the response epoch were classified as having “peri-movement selectivity.” Neurons that were selective during the delay epoch were further classified into ‘contra-preferring neurons’ if total spike counts during the delay epoch was higher in contra-trials (or ‘ipsi-preferring neurons’ if the total spike counts during the delay epoch was higher in ipsi-trials). Only correct trials were included to classify neurons.

To compute ‘contra-selectivity’, we took the firing rate difference between the contra-trials and ipsi-trials for each neuron. To compute ‘normalized contra-selectivity’ we normalized the contra-selectivity by its peak value (Figures 4E, S2C, and S2I). The averaged selectivity was the mean firing rate difference between the preferred trials and non-preferred trials (Figures 2, 3, 4, 5, 6, 7, S3–S5, S7, and S8). To analyze the effect of optogenetic perturbation on selectivity, units with at least 6 inactivation or activation trials were selected (Figures 2, 3, 4, 6, 7, S3–S5, S7, and S8). We used the last 300 ms to quantify the effect of perturbation if not specified.

For the peri-stimulus time histograms (PSTHs; Figures 2, 3, 4, 6, 7, S3–S5, S7, and S8), correct and incorrect trials were included, as optogenetic perturbations changed neural activity irrespective of the response outcomes. Spikes were averaged over 100 ms with 1 ms bin. Bootstrapping was used to estimate standard errors of the mean (Figures 2, 3, 4, 6, 7, S3–S5, S7, and S8).

To compute mean firing rate of a neuron, the spikes in contra- and ipsi-trials were combined (correct and incorrect trials, units with at least 6 optogenetic perturbation trials; Figures 2, 3, 4, 6, 7, S3–S5, S7, and S8). We also tested a range of numbers of trials (from 2 to 15) and the results were similar. The Student’s *t* test was used to determine whether the neuron significantly changed its mean firing rate during perturbation relative to the control firing rate without perturbation ($p < 0.05$). To differentiate the pattern of significantly modulated neurons, we used the *chi-square* test to compare the fraction of significantly up-modulated neurons in contra-preferring and ipsi-preferring neurons (relative to the total significantly modulated neurons in each group) (Figures 2, 3, 6, 7, S3–S5, S7, and S8).

The onset of inactivation was calculated as when the PSTHs during the inactivation and control conditions were significantly different (*t* test, the first time point when 3 continuous time points were significantly different; Figure S3M). Changing the number of continuous time points (3–10) did not change the estimated latency. The PSTHs were computed with 1 ms bin and smoothed with 10 ms. To estimate the standard error of mean, we randomly sampled neurons with replacement and used the bootstrapped data to compute the onset of inactivation. This procedure was repeated 1000 times.

To determine whether a neuron encoded sensory input or movement, we compared the selectivity in the correct and incorrect trials (Figure S7) (Inagaki et al., 2018). r and θ were defined as below.

$$r = \sqrt{\text{Selectivity in correct trials}^2 + \text{Selectivity in incorrect trials}^2}$$

$$\theta = \tan^{-1} \left(\frac{\text{Selectivity in correct trials}}{\text{Selectivity in incorrect trials}} \right)$$

Neurons with more than 6 incorrect trials for each trial-type and $r > 2$ were selected for the analysis of θ . If the selectivity in correct trials and incorrect trials was the same, i.e., the neuron encoded sensory input and its selectivity was not affected by the animal’s choice, then $\theta = 45^\circ$. To analyze neurons that encoded sensory input, we selected neurons with the θ between 22.5° and 67.5° (Figures S7G and S7H).

The coding direction (CD) is a n dimensional vector in activity space that maximally distinguish contra-trials and ipsi-trials (Li et al., 2016). For each session, we randomly selected half of trials to compute CD in the last 500 ms of the delay epoch and project the remaining half of trials to the CD to obtain trajectories (Figures 2, 3, 6, 7, S3–S5, S7, and S8). Sessions with at least 6 simultaneously recorded neurons and at least 8 trials for each trial types (contra-trials and ipsi-trials during control and perturbation conditions) were selected. The neural trajectories were smoothed with a 200 ms time window.

Decoding of sensory, choice and outcome information

To quantify the coding capability of sensory, choice and outcome information of individual neurons, we first randomly selected n trials from each of the 4 trial types (lick-left correct, lick-left error, lick-right correct and lick-right error trials, $n = 10$ for each trial type, neurons with less than 10 trials for each trial type were not selected). We then calculated firing rates during the sample or delay epoch for each selected trial. The coding of sensory information (i.e., weak or strong stimuli in lick-left or lick-right trials) was determined by comparing firing rates between lick-left trials and lick-right trials (n lick-left correct trials and n lick-left error trials versus n lick-right correct trials and n lick-right error trials). The coding of choice information was determined by comparing firing rates between trials that mice licked left and trials that mice licked right (n lick-left correct trials and n lick-right error trials versus n lick-left error trials and n lick-right correct trials). The coding of outcome information was determined by comparing firing rates between trials that mice obtained reward and trials that mice performed incorrectly (n lick-left correct trials and n lick-right correct trials versus n lick-left error trials and n lick-right error trials). To quantify the difference between firing rates in selected groups of trials, we first drew the receiver operating characteristic curve (ROC), and then calculated the area under the curve (AUC). If AUC was 0.5, it meant the fraction of false positive and false negative predictions were the same and thus the neuron did not encode information. If AUC was close to 1, the neuron discriminated trials nearly perfectly. If AUC was less than 0.5, we would subtract its value from 1 to get the final AUC. To get the standard deviation of AUC, we repeated the above steps 200 times. We then averaged AUC values to obtain the coding capability of sensory, choice and outcome information for each neuron.

To quantify the coding capability of selected population of neurons, we trained a support vector machine (SVM) classifier using ten-fold cross-validation (fitcecoc function in MATLAB from Mathworks). Because the number of simultaneously recorded neurons was limited in a session, we constructed a pseudo-population for the SVM classifier in the following steps. 1) Neurons from different recording sessions were pooled together. 2) A set of n neurons were randomly selected (n was variable to obtain a relationship between decoding accuracy and number of neurons). 3) A set of m trials were randomly selected from each of the 4 trial types (lick-left correct, lick-left error, lick-right correct and lick-right error trials, $m = 10$ for each trial type, neurons with less than 10 trials for each trial type were not selected). 4) The firing rate of each selected neuron was calculated for each trial type to form an $n \times 4 \times m$ matrix. 5) A SVM algorithm was trained to classify different trials types (lick-left versus lick-right trials for sensory information, lick-left versus lick-right choice for decision information, and correct versus error trials for outcome information). The classification accuracy was obtained through m -fold cross-validation. That is, the data was evenly divided into m parts, and the model was trained with $m-1$ parts, and then the remaining part was used as testing dataset. This process was repeated m times to obtain the averaged classification accuracy. 6) To get the corresponding standard deviation, steps 2–5 were repeated 200 times. 7) To quantify the decoding accuracy as a function of the number of neurons, the number of selected neurons was varied between 1 and 500 and steps 2–6 were repeated to get the decoding accuracy for each value of n . As $n = 200$ yielded good prediction, we used this fixed number of neurons to quantify the decoding accuracy at different time points along trial progression (step size, 50 ms; smoothing window, 100 ms).

To obtain noise correlation of a pair of simultaneously recorded neurons, we first subtracted mean activity from their trial-to-trial activity and calculated the Pearson correlation.

$$NC_{ij} = \frac{\text{cov}(u_i, u_j)}{\sqrt{\text{var}(u_i) \times \text{var}(u_j)}}$$

u_i and u_j represents the activity of the i -th and j -th neuron, respectively. Activity in lick-left and lick-right trials were concatenated to form a one-dimensional vector (including the sample and delay epochs with bin size 100 ms). $\text{cov}(u_i, u_j)$ represents the covariance of u_i and u_j . For control, we shuffled the labels of these trials before concatenating them to form the one-dimensional vector. Signal correlation was the Pearson correlation of the mean activity of these neurons.

Optical tagging of SNr GABAergic neurons

Gad2-IRES-Cre \times R26-CAG-LSLReaChR-mCitrine mice were used for optical tagging. A small craniotomy (diameter, 2 mm) was made over the ipsilateral visual cortex (center relative to bregma: AP -3.2 , ML -3.5 mm) one day prior to the recording session. An optrode (Cambridge NeuroTech) with an optic fiber (100 μm diameter, 500 μm away from the electrode tips) was driven down about 4 mm at 30° to reach SNr. In some sessions, the laser (10 mw, 1 Hz, lasting for 20 ms, randomly selected in 80% of trials) was given 3 times in each trial. In some sessions, the laser (lasting for 50 ms) was given only at the beginning of the trial. There were typically 4 recording sessions per probe penetration and each session lasted for about 300 trials. Between sessions (lasting for ~ 5 mins), the probe was driven 250 μm deeper by a micromanipulator (MP285, Sutter Instrument). Before withdrawing the probe, a mild current delivered by an electric stimulator (30 μA , 1 s, 6 times, Digitimer DS3, Welwyn Garden City, UK) was used to mark a small lesion at the recording location.

We isolated 163 SNr units from 9 recording sessions. To identify the laser-responsive neurons, we used two-sample t test to compare the spikes between control and photo-stimulation conditions in each 1 ms bin (tested from 1–6 ms). Tagged neurons were selected as laser-responsive if they were significantly activated within 6 ms ($p < 0.05$), and have high correlation coefficients in spike waveform between control and stimulation conditions (> 0.9). The response latency was the first time bin to show significantly increased firing rate above control. We identified 21 laser-responsive neurons. Among these, 13 and 1 neurons were classified as FS and wide spiking neurons respectively. Spike widths of the remaining 7 neurons were in the range from 0.4 to 0.6 ms. These results confirmed that SNr mainly contained neurons with narrow spikes. We focused on neurons with spike width < 0.4 ms, but the results were similar when including neurons with spike width > 0.4 ms (data not shown).

Statistics

The sample sizes are similar or larger to sample sizes typically used in the field (more than 100 units per brain region). No statistical methods were used to determine sample size. We did not exclude any animal for data analysis. Trial types were randomly determined by a computer program. During spike sorting, experimenters cannot tell the trial type, so experimenters were blind to conditions. All comparisons using t tests are two-sided. All bootstrapping was done over 1,000 iterations. See the above sections on [Behavioral data analysis](#) for details of statistics.

Neuron, Volume 109

Supplemental information

**A cortico-basal ganglia-thalamo-cortical
channel underlying short-term memory**

Yu Wang, Xinxin Yin, Zhouzhou Zhang, Jiejue Li, Wenyu Zhao, and Zengcai V. Guo

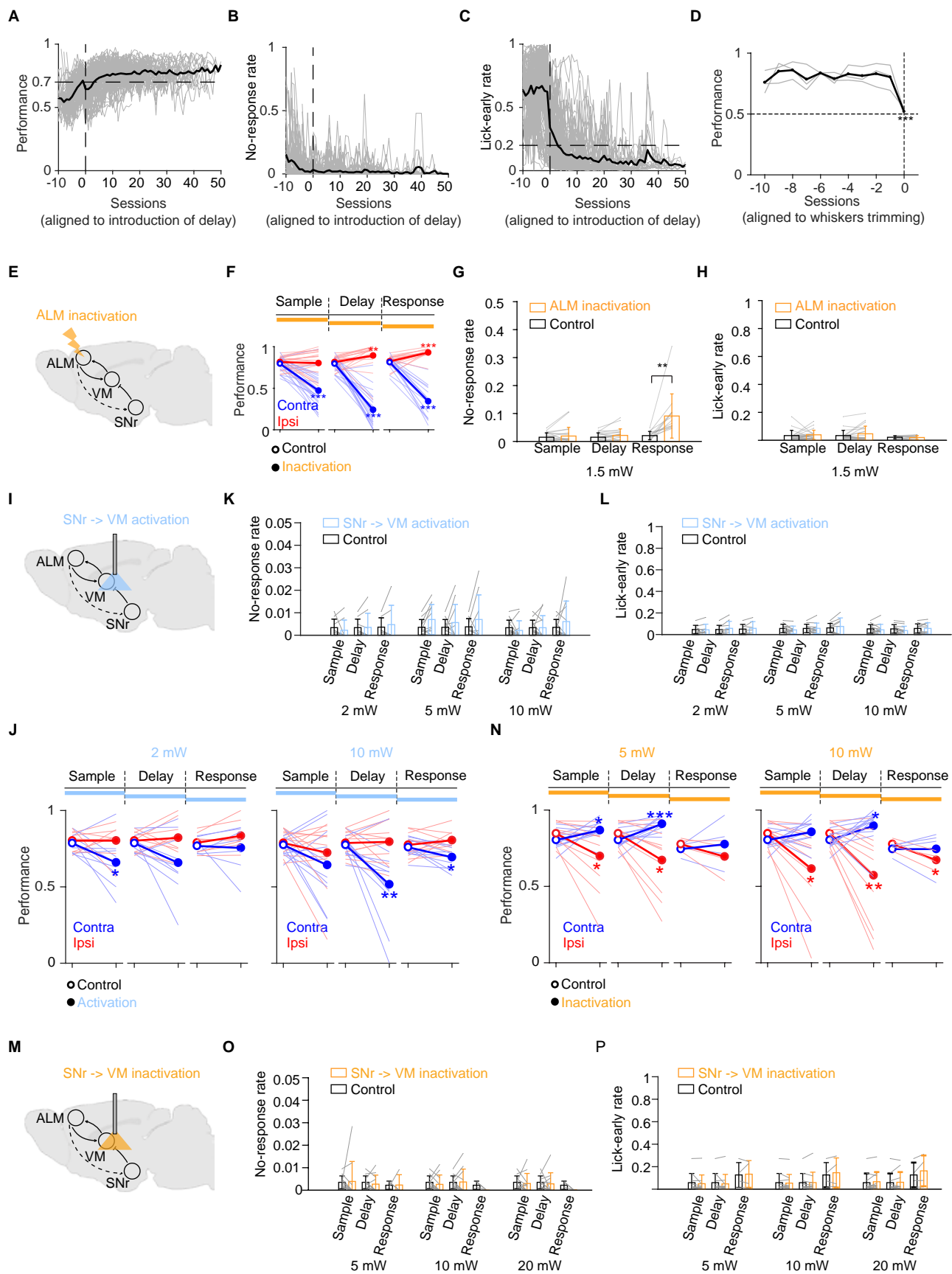


Figure S1. Behavioral training process and optogenetic perturbation deficits, related to Figure 1.

- A.** Learning curves ($n = 104$ mice). Sessions were aligned to the final step of training (i.e. adding the delay epoch, see Methods). Thick line, mean performance; thin lines, individual mice.
- B.** No-response rate. Same mice as in **A**.
- C.** Lick-early rate. Same mice as in **A**.
- D.** Performance was reduced to chance level after whiskers trimming ($n = 3$ mice). Thick line, mean performance; dotted lines, individual mice.
- E.** Schematic of ALM inactivation.
- F.** Performance change after unilateral ALM inactivation (left hemisphere, $n = 21$ mice). Thick line, mean performance; thin lines, individual mice.
- G.** Inactivation of ALM did not increase no-response rate during the sample or delay epoch. There was a small increase in no-response rate during the response epoch (from $2.1 \pm 1.5\%$ to $9.1 \pm 8.0\%$, mean \pm SEM, t -test, $p < 0.01$).
- H.** Inactivation of ALM did not increase lick-early rate.
- I.** Schematic of activation of SNr projections in VM. Same as Figure 1C.
- J.** Performance during control (without activation) and activation at different laser powers (8 mice for 2 mw, 11 mice for 10 mw).
- K.** Activation did not increase no-response rate.
- L.** Activation did not increase lick-early rate.
- M.** Schematic of inactivation of SNr projections in VM. Same as Figure 1G.
- N.** Performance during control (without inactivation) and inactivation at different laser powers ($n = 10$ mice).
- O.** Inactivation did not increase no-response rate.
- P.** Inactivation did not increase lick-early rate.

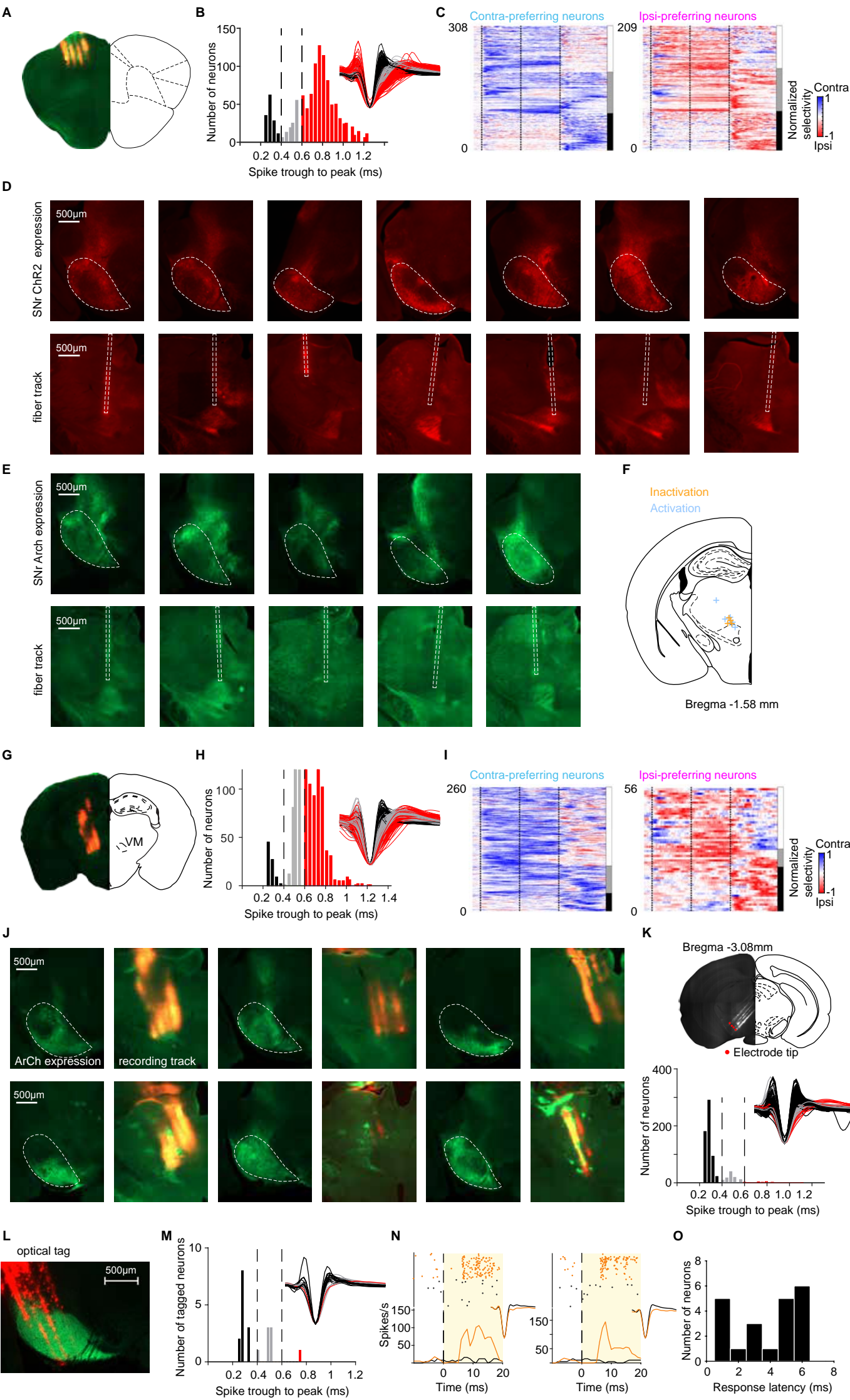


Figure S2. Recording locations, fiber tracts and neuron response types in ALM, thalamus and SNr, related to Figures 1-6, Figures S3, S5-7.

- A.** Example electrode tracks labelled with DiI (red) in ALM.
- B.** Single-unit classification in ALM recorded using 64-channel silicon probes (including units recorded during SNr activation or inactivation). Putative fast-spiking interneurons (black, $n = 136$) and putative pyramidal neurons (red, $n = 771$) were separated on the basis of the bimodal distribution of spike widths (Methods). A small subset of neurons with intermediate spike durations were not classified ($n = 179$). Right, mean spike waveform of each unit.
- C.** ALM population selectivity ($n = 517$). Vertical bars on the right: white, neurons with preparatory activity only; grey, neurons with both preparatory activity and peri-movement activity; black, neurons with peri-movement activity only. Units switched preference in different epochs were excluded.
- D.** Viral expression of optogenetic activator ChR2 in SNr (top). Bottom, expression of axon terminals in VM and fiber track.
- E.** Viral expression of optogenetic silencer Arch in SNr (top). Bottom, expression of axon terminals in VM and fiber track.
- F.** Fiber tip locations in optogenetic activation and inactivation experiments.
- G.** Example electrode tracks in the thalamus.
- H.** Single-unit classification in the thalamus. Putative thalamic neurons (red, $n = 570$) were selected on the basis of the bimodal distribution of spike widths (Methods). Right, mean spike waveform of each unit.
- I.** Thalamic population selectivity ($n = 316$). Same format as in **C**.
- J.** Viral expression of optogenetic silencer (Arch) in SNr and electrode tracks in the thalamus.
- K.** Single-unit classification in the SNr. Top, example electrode tracks in the SNr. Bottom, distribution of spike widths (trough to peak). Putative GABAergic neurons (black, $n = 611$) were selected on the basis of the narrow spike widths (Methods). Right, mean spike waveform of each unit.
- L.** Example electrode tracks in experiments of optical tagging.
- M.** Distribution of spike widths of tagged cells ($n = 21$ out of 163 neurons).
- N.** Example tagged neurons. Spike raster and PSTH are shown during optical stimulation (orange) and control (black). Inset, mean spike waveform during stimulation (orange) and control (black). Dashed line, start of optical stimulation. Orange shading, duration of light. Bin size, 1 ms. Averaging window, 3 ms.
- O.** Distribution of response latency. Mean latency, 3.9 ± 2 ms (mean \pm SD, $n = 21$).

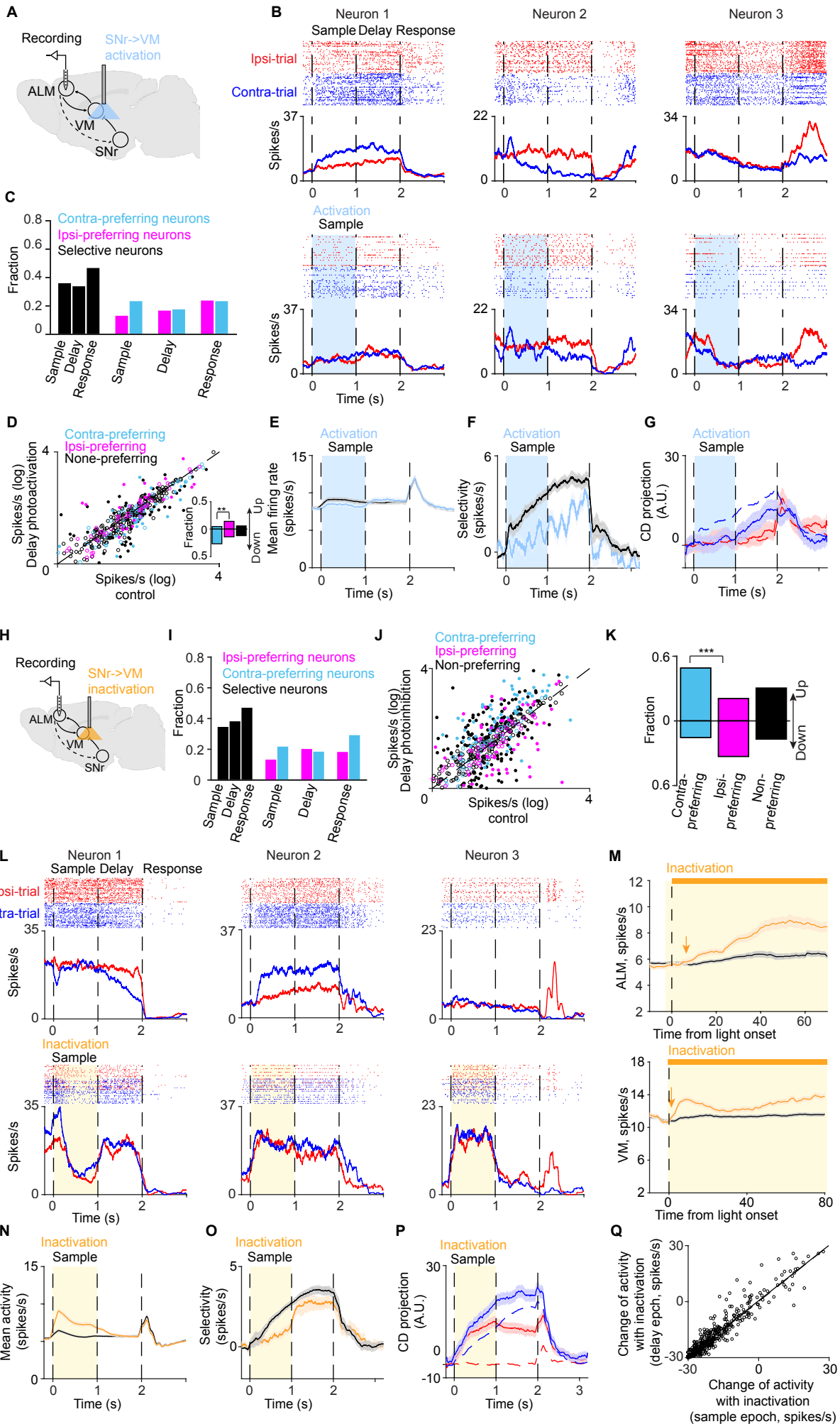


Figure S3. Activation or inactivation of SNr->thalamus axons during the sample epoch selectively modulates ALM activity, related to Figures 2-3.

- A.** Schematic of recording in ALM during optogenetic activation of SNr axons near VM (same as Figure 2A).
- B.** Three example ALM neurons during SNr terminal activation for the sample epoch (same neurons as in Figure 2B). Top: spike raster and peri-stimulus time histogram (PSTH). Bottom: spike raster and PSTH during SNr terminal activation. Bin size, 1ms. Averaging window, 100ms. Correct contra- (blue) and ipsi- (red) trials only. Dashed lines separate behavioral epochs.
- C.** Fraction of selective ALM neurons during the sample, delay or response epoch.
- D.** Scatter plot of mean firing rates during the sample epoch. Cyan, right-preferring neurons. Magenta, left-preferring neurons. Black, non-preferring neurons. Filled circles, neurons are significantly modulated ($P < 0.05$, t -test). Dotted line is the unity line. Inset, fraction of up-modulated neurons and down-modulated neurons.
- E.** Mean PSTH of ALM neurons during control (black) and SNr terminal activation (blue). Shading, SEM.
- F.** Selectivity of ALM neurons during control (black) and SNr terminal activation (blue).
- G.** Coding direction projected activity during control (dotted) and SNr terminal activation (solid lines). Shading, SEM ($n = 7$ mice). Bin size, 1 ms. Averaging window, 200ms.
- H.** Schematic of recording in ALM during inactivation of SNr terminals near VM (same as Figure 3A).
- I.** Fraction of selective ALM neurons during the sample, delay or response epoch.
- J.** Scatter plot of mean firing rates during the sample epoch. Cyan, right-preferring neurons. Magenta, left-preferring neurons. Black, non-preferring neurons. Filled circles, neurons are significantly modulated ($P < 0.05$, t -test). Dotted line is the unity line.
- K.** Fraction of up-modulated neurons and down-modulated neurons in each group shown in **J**.
- L.** Three example ALM neurons during SNr terminal inactivation (same neurons as in Figure 3B). Top: spike raster and peri-stimulus time histogram (PSTH). Bottom: spike raster and PSTH during SNr terminal inactivation. Bin size, 1ms. Averaging window, 100ms. Correct contra- (blue) and ipsi- (red) trials only. Dashed lines separate behavioral epochs.
- M.** Onset of activity change in ALM (top) or thalamic (bottom) neurons. Black, control PSTH without inactivation. Orange, PSTH with inactivation of SNr terminals. Shading, SEM. Arrow, onset of activity increase in ALM (top) or thalamus (bottom).
- N.** Mean PSTH of ALM neurons during control (black) and SNr terminal inactivation (orange). Shading, SEM.
- O.** Selectivity of ALM neurons during control (black) and SNr terminal inactivation (orange).
- P.** Coding direction projected activity during control (dotted) and SNr terminal inactivation (solid lines). Shading, SEM ($n = 5$ mice). Bin size, 1 ms. Averaging window, 200ms.
- Q.** Change of ALM activity induced by SNr inactivation during the delay epoch is linearly correlated with that during the sample epoch inactivation.

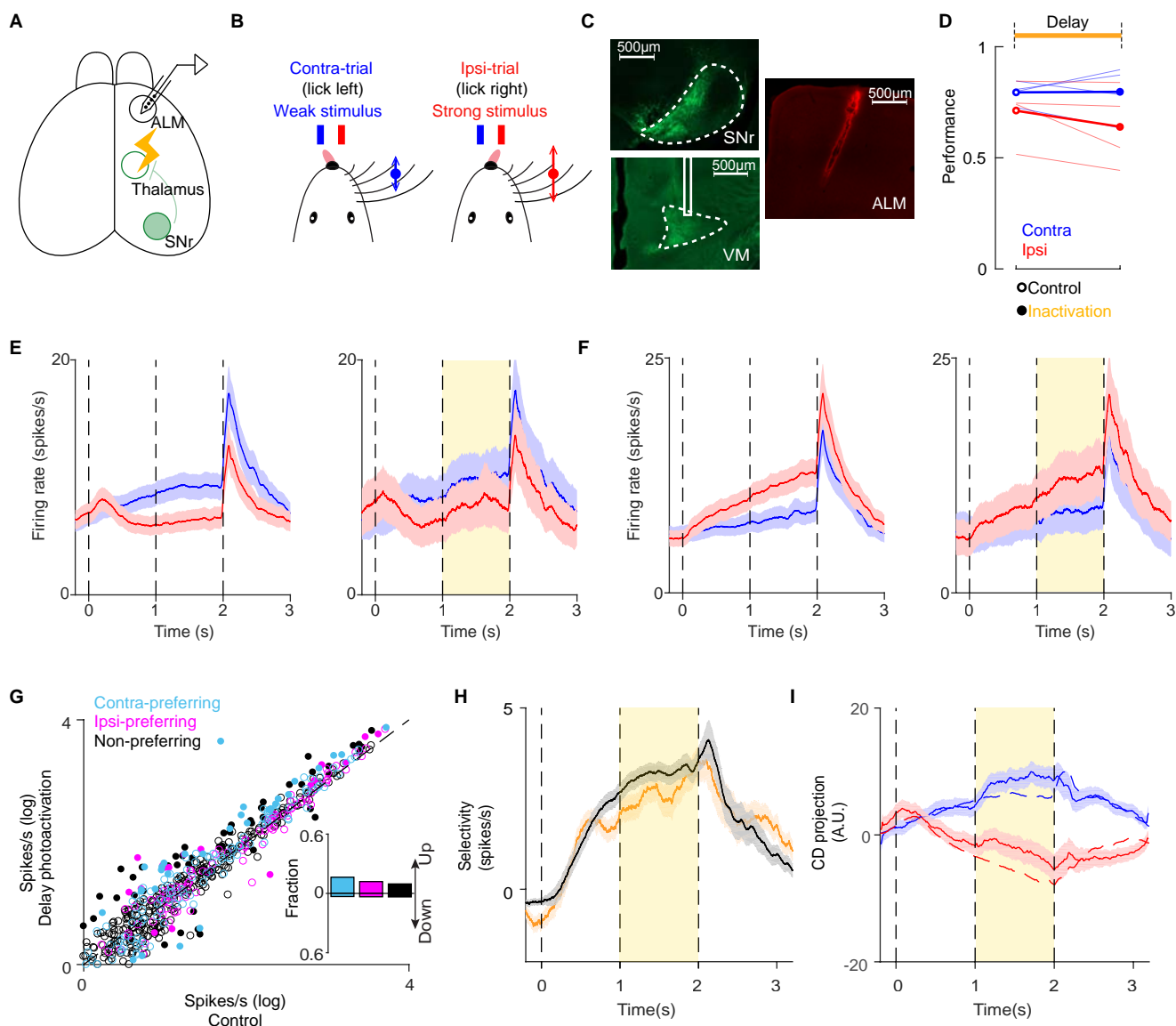


Figure S4. Behavioral performance and ALM activity change during inactivation of SNr-> thalamus terminals in the right hemisphere, related to Figure 3.

- A.** Schematic of recording in ALM during optogenetic inactivation of SNr axons near VM in the right hemisphere.
- B.** Schematic of the behavior. Contra- and ipsi- denote the side relative to optogenetically perturbed right hemisphere.
- C.** Viral expression of optogenetic activator ChR2 in the right SNr (top). Bottom, expression of axon terminals in VM and fiber track. Right, track of the recording probe in the right ALM.
- D.** Performance during control and optogenetic inactivation of the right SNr terminals near VM (n = 4 mice).
- E.** Mean PSTH of ALM contra-preferring neurons during control (left) and optogenetic inactivation (right). n=177 neurons from 4 mice. Shading, SEM.
- F.** Mean PSTH of ALM ipsi-preferring neurons during control (left panel) and optogenetic inactivation (right panel). n=139 neurons from 4 mice. Shading, SEM.
- G.** Scatter plot of mean firing rates during the delay epoch (n = 866 neurons from 4 mice). Same format as in Figure 2C. Inset, fraction of up-modulated neurons and down-modulated neurons in each group.
- H.** Selectivity of ALM neurons during control (black) and perturbations (orange).
- I.** Projections along the coding direction during control (dotted) and perturbations (solid lines). Shading, SEM

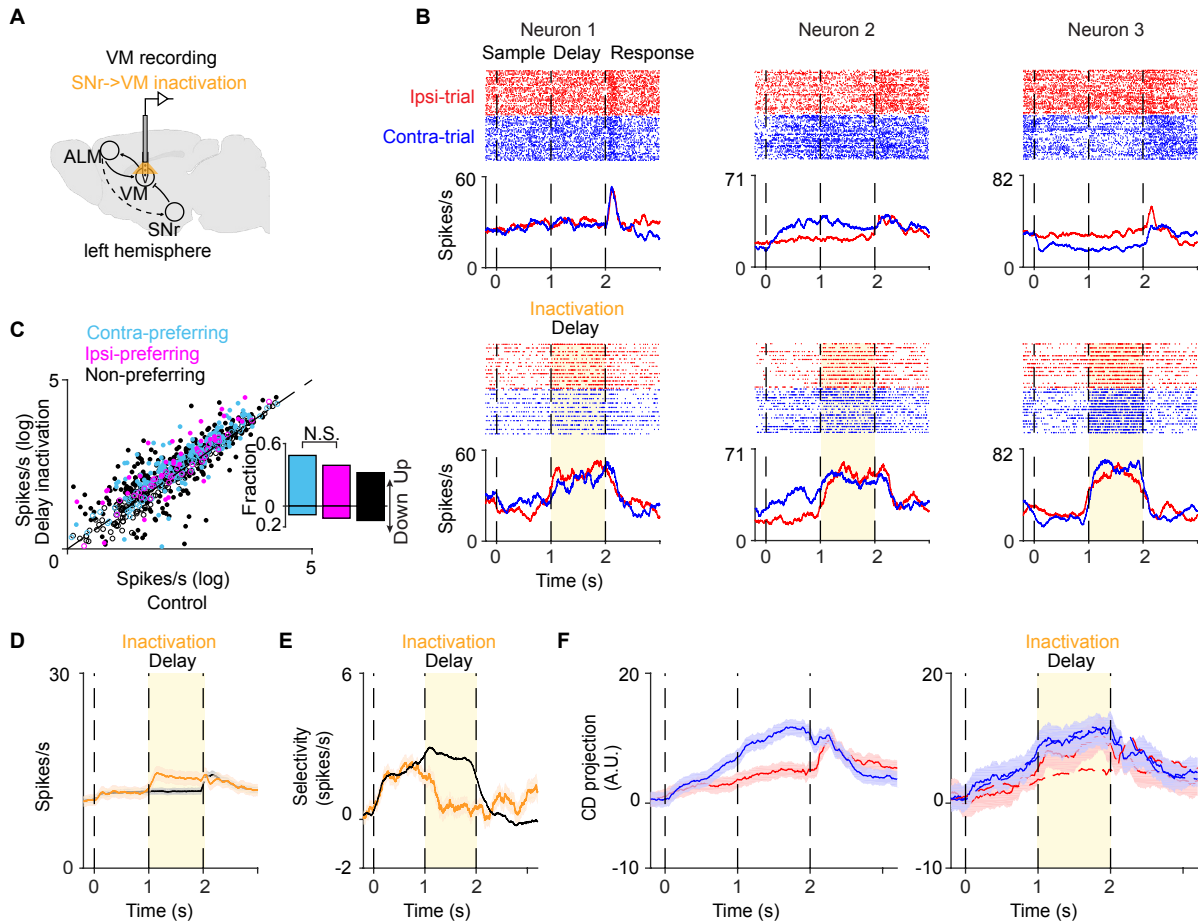
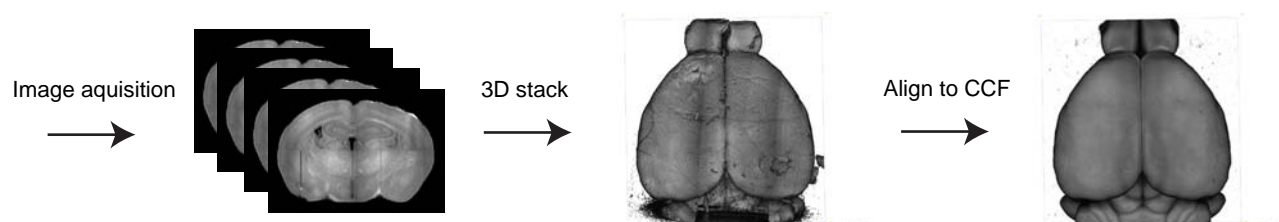


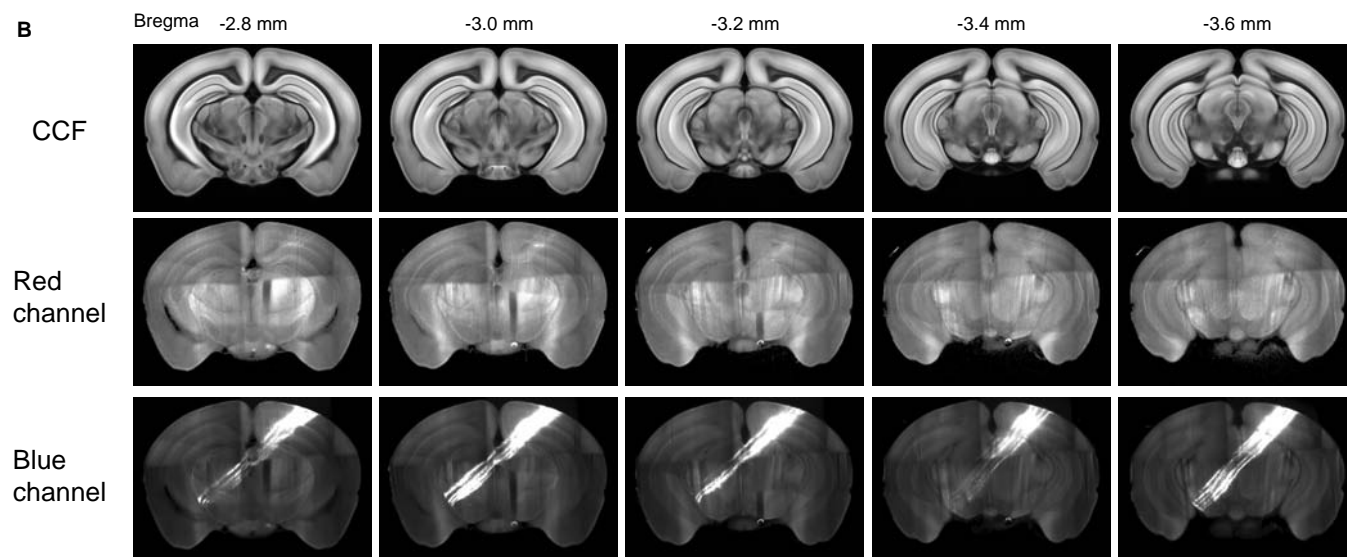
Figure S5. Inactivation of SNr->thalamus axons selectively modulates thalamic activity, related to Figure 3.

- Schematic of recording in the thalamus near VM/VAL during inactivation of SNr terminals.
- Three example neurons in the thalamus during SNr terminal inactivation. Top: spike raster and peri-stimulus time histogram (PSTH). Bottom: spike raster and PSTH during SNr terminal inactivation. Bin size 1ms. Averaging window 100ms. Correct contra- (blue) and ipsi- (red) trials only. Dashed lines separate behavioral epochs.
- Scatter plot of mean firing rates during the delay epoch (570 neurons from 6 mice). Cyan, right-preferring neurons. Magenta, left-preferring neurons. Black, non-preferring neurons. Filled circles, neurons are significantly modulated ($p < 0.05$, t -test). Dotted line is the unity line. Inset, fraction of up-modulated neurons and down-modulated neurons in each group. N.S., non-significant (chi-square test).
- Mean PSTH of thalamic neurons during control (black) and SNr terminal inactivation (orange). Shading, SEM.
- Selectivity of thalamic neurons during control (black) and SNr terminal inactivation (orange).
- Coding direction projected activity during control (dotted) and SNr terminal inactivation (solid lines). Shading, SEM ($n = 20$ mice). Bin size, 1 ms. Averaging window, 200ms.

A

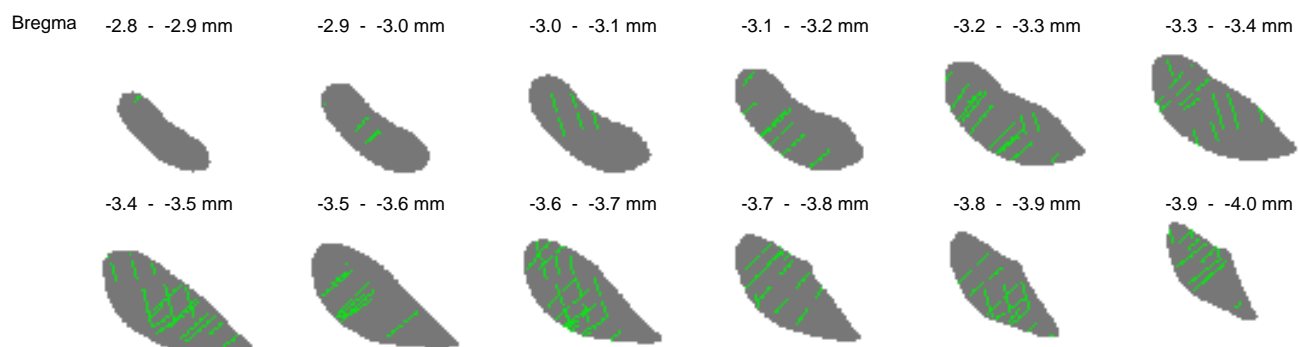


B



C

Recording sites locations



D

Recording densities

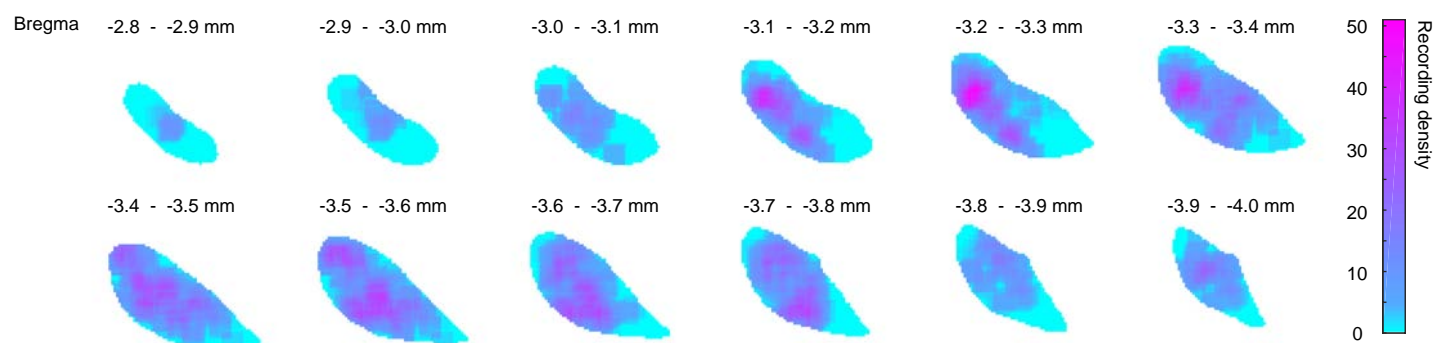


Figure S6. 3D imaging and reconstruction of electrode tracks, related to Figures 4-6.

- A.** The pipeline for 3D reconstruction and alignment of electrode tracks.
- B.** Example slices showing the aligned electrode tracks. CCF: common coordinate framework (<http://atlas.brain-map.org/>). Red channel, excitation at 647nm used to align images to the CCF. Blue channel, excitation at 488nm used to image DiI signal.
- C.** Reconstructed electrode tracks at different coronal slices in SNr.
- D.** Recording density at different coronal sections (see Methods). Slices from Bregma -2.8 to -3.8mm are shown in Figure 4F.

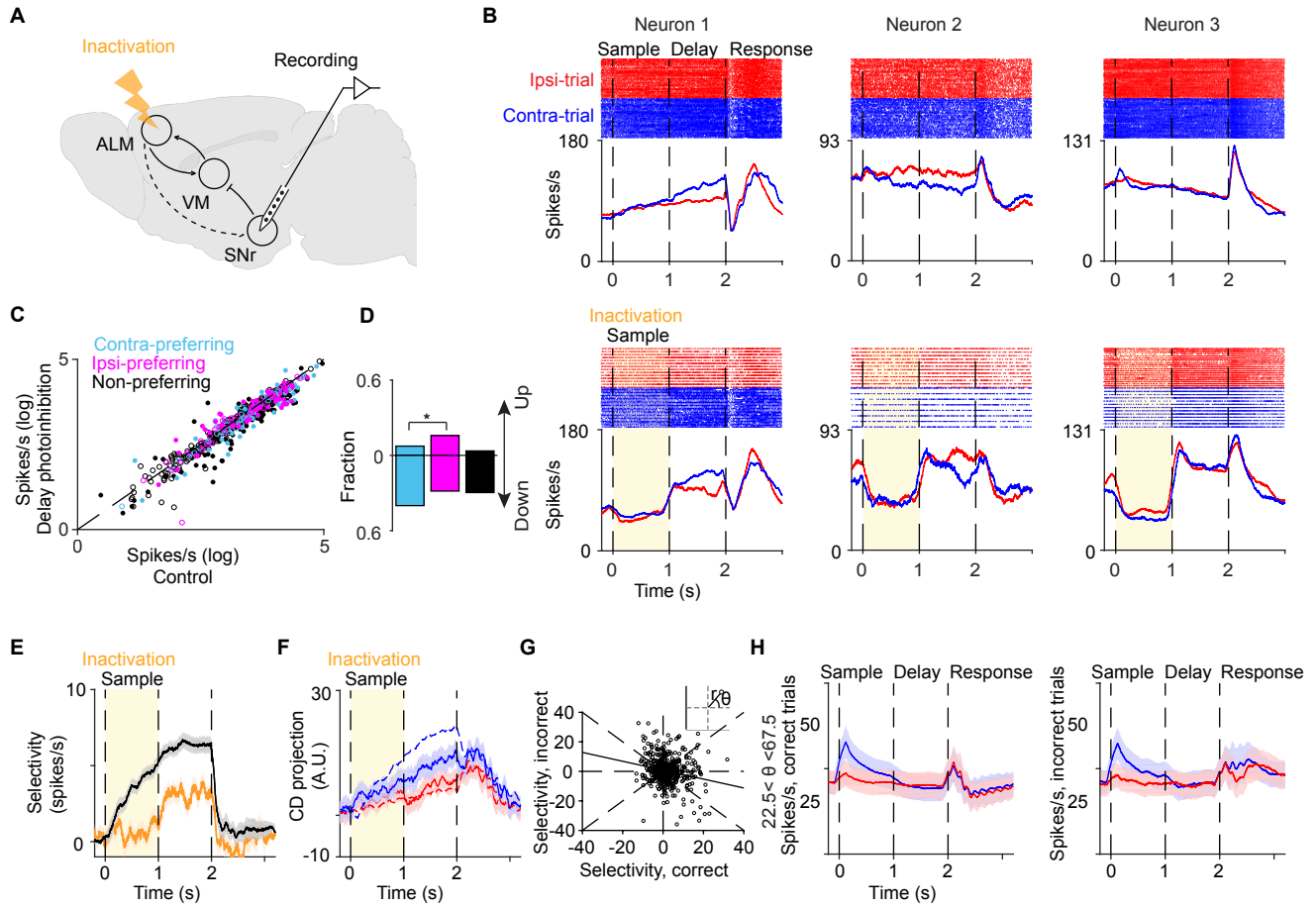


Figure S7. Inactivation of ALM during the sample epoch selectively modulates SNr activity, related to Figure 6.

- A.** Schematic of recording in SNr during ALM inactivation. Same as Figure 6A.
- B.** Three example SNr neurons during ALM inactivation during the sample epoch (same neurons as in Figure 6B). Top: spike raster and PSTH. Bottom: spike raster and PSTH during ALM inactivation. Bin size 1ms. Averaging window 100ms. Correct lick-right (blue) and lick-left (red) trials only. Dashed lines separate behavioral epochs.
- C.** Scatter plot of mean firing rates during the sample epoch. Same format as in Figure 6C.
- D.** Fraction of up-modulated neurons and down-modulated neurons in each group of neurons.
- E.** Selectivity of SNr neurons during control (black) and ALM inactivation (orange).
- F.** Coding direction projected activity during control (dotted) and ALM inactivation (solid lines). Inactivation of ALM biased neural trajectory in contra-trials (blue) to that in ipsi-trials (red).
- G.** Scatter plot of selectivity in correct and error trials. Line, linear regression. See Methods for definition of r and θ .
- H.** Mean PSTH of sensory-related SNr neurons in correct (left) and error (right) trials ($n = 58$ neurons). Sensory-related neurons are those showing similar response in correct and error trials (dots with θ between 22.5° and 67.5° , see Methods).

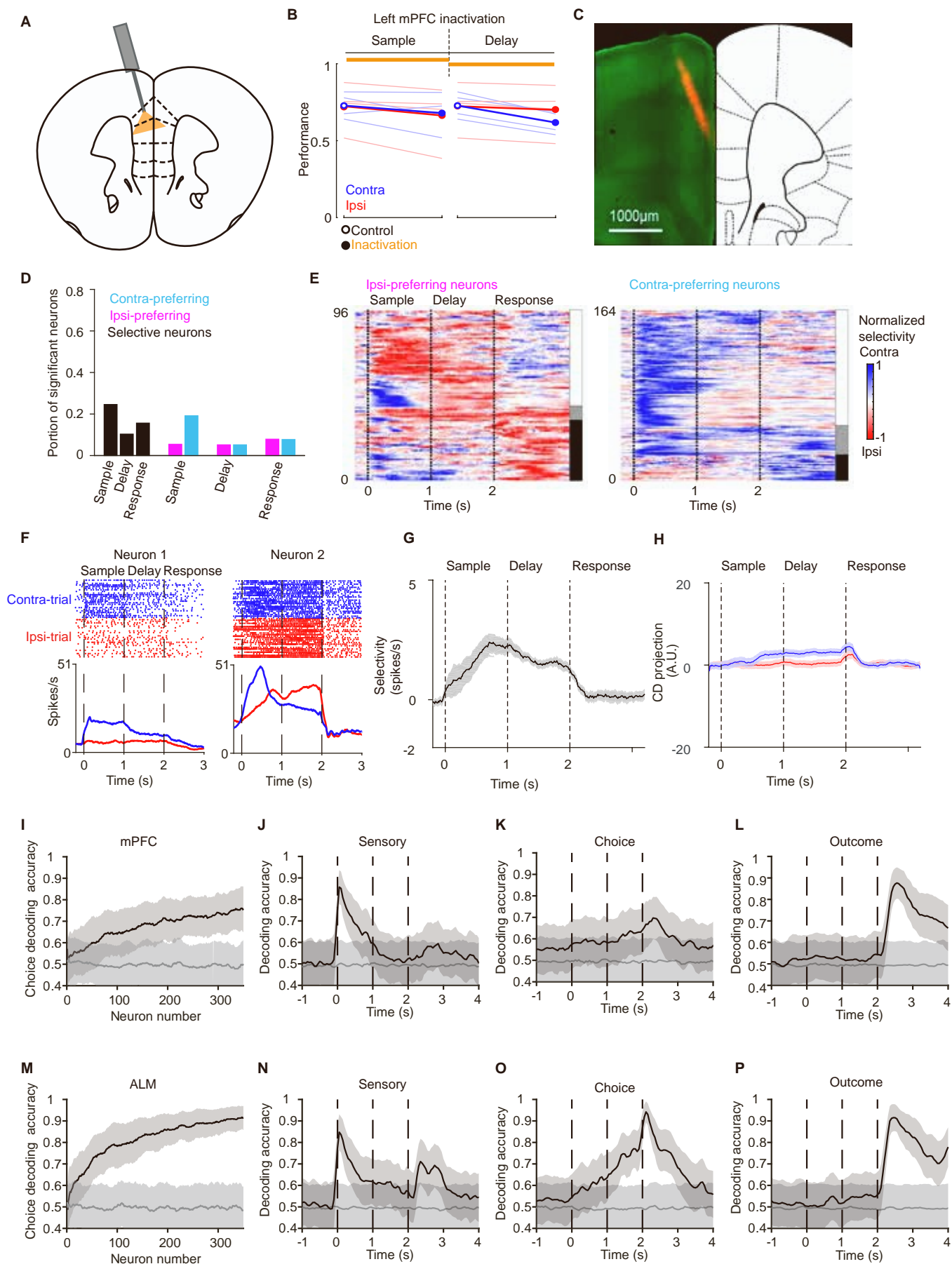


Figure S8. mPFC is not necessary for STM in the tactile based decision task, related to Figures 1, 4 and 5.

- A.** Schematic of optogenetic inactivation of the left mPFC through an implanted optical fiber.
- B.** Inactivation of left mPFC during the delay epoch affected task performance little ($n = 4$ mice).
- C.** Example DiI track of the recording probe.
- D.** Fraction of neurons that are significantly modulated during different behavior epochs (sample, delay and response). The fraction is much smaller than that in ALM for each epoch (ALM vs mPFC, sample epoch: 34.1% vs 24.6%, $p < 0.001$, chi-square test; delay epoch: 37.8 vs 10.3%, $p < 0.001$; response epoch: 46.6% vs 15.7%, $p < 0.001$).
- E.** Population selectivity that is normalized to its peak (96 ipsi-preferring neurons and 164 contra-preferring neurons). Vertical bars on the right: white, neurons with preparatory activity only; grey, neurons with both preparatory activity and peri-movement activity; black, neurons with peri-movement activity only.
- F.** Example mPFC neurons. Top: spike raster. Bottom: PSTH. Bin size, 1ms. Averaging window, 100ms. Correct lick-right (blue) and lick-left (red) trials only. Dashed lines separate behavioral epochs.
- G.** Mean selectivity of delay-selective neurons in mPFC. Black, Mean. Shading, SEM.
- H.** Projection of neural trajectories along CD. The separation between the ipsi-trajectory and contra-trajectory is significantly smaller than that in ALM (1.5 ± 0.5 vs 7.7 ± 0.2 , bootstrap, $p < 0.001$).
- I.** The accuracy of choice increases with the number of randomly selected neurons (see Methods). Light line, control with trial labels shuffled. Shading, standard deviation.
- J.** The decoding accuracy of sensory information along trial progression based on 200 randomly selected neurons with balanced trial types (see Methods). Light line, control with trial labels shuffled. Shading, standard deviation.
- K.** The decoding accuracy of choice. Same format as in J.
- L.** The decoding accuracy of outcome. Same format as in J.
- M-P.** Decoding of sensory, choice and outcome information using neurons in ALM. Same format as in I-L.